DIFFUSION MODELS ALREADY HAVE A SEMANTIC LATENT SPACE

Anonymous authors
Paper under double-blind review

ABSTRACT

Diffusion models achieve outstanding generative performance in various domains. Despite their great success, they lack *semantic* latent space which is essential for controlling the generative process. To address the problem, we propose **asy**mmetric **r**everse **p**rocess (Asyrp) which discovers the semantic latent space in *frozen* pretrained diffusion models. Our semantic latent space, named *h-space*, has nice properties to accommodate semantic image manipulation: homogeneity, linearity, robustness, and consistency across timesteps. In addition, we introduce a principled design of the generative process for versatile editing and quality boosting by quantifiable measures: *editing strength* of an interval and *quality deficiency* at a timestep. Our method is applicable to various architectures (DDPM++, iDDPM, and ADM) and datasets (CelebA-HQ, AFHQ-dog, LSUN-church, LSUN-bedroom, and METFACES).

1 INTRODUCTION

In image synthesis, diffusion models have advanced to achieve state-of-the-art performance regarding quality and mode coverage since the introduction of denoising diffusion probabilistic models (Ho et al., 2020). They disrupt images by adding noise through multiple steps of forward process and generate samples by progressive denoising through multiple steps of reverse (i.e., generative) process. We refer to the intermediate noisy images as latent variables. Since their deterministic version enables nearly perfect reconstruction of input images (Song et al., 2020a), they are suitable for image editing, which renders target attributes on the real images. However, simply editing the latent variables causes degraded results (Appendix D5 in Kim & Ye (2021)). Instead, they require complicated procedures: providing guidance in the reverse process or finetuning models for an attribute.

Figure 1(a-c) briefly illustrates the existing approaches. Image guidance mixes the latent variables of the input image with unconditional latent variables (Choi et al. (2021), Lugmayr et al. (2022), Meng et al. (2021)). Though it provides some control, it is ambiguous to specify which attribute to reflect among the ones in the input and unconditional result and it lacks intuitive control for the magnitude of change. Classifier guidance manipulates images by imposing gradients of a classifier on the latent variables in the reverse process to match the target class (Dhariwal & Nichol (2021), Avrahami et al. (2022), Liu et al. (2021)). It requires training an extra classifier for the latent variables, i.e., noisy images. Furthermore, computing gradients through the classifier during sampling is costly. Finetuning the whole model can steer the resulting images to the target attribute without the above problems (Kim & Ye, 2021). Still, it requires multiple models to reflect multiple descriptions.

On the other hand, generative adversarial networks (Goodfellow et al., 2020) inherently provide straightforward image editing in their latent space. Given a latent vector for an original image, we can find the direction in the latent space that maximizes the similarity of the resulting image with a target description in CLIP embedding (Patashnik et al., 2021). The latent direction found on one image leads to the same manipulation of other images. However, given a *real* image, finding its exact latent vector is often challenging and produces unexpected appearance changes.

It would allow admirable image editing if the diffusion models with the nearly perfect inversion property have such a semantic latent space. Preechakul et al. (2022) introduces an additional input to

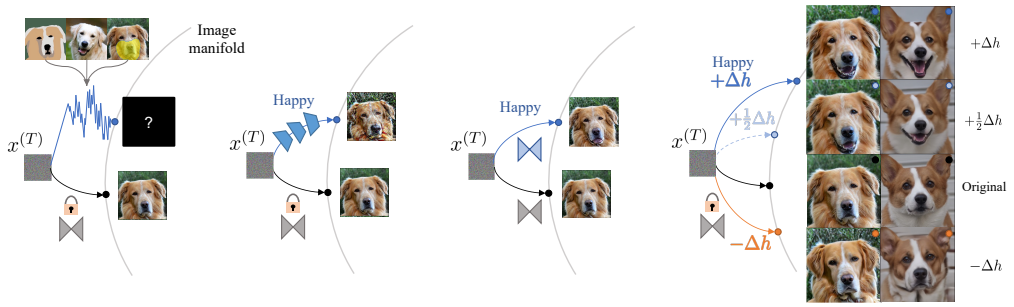

(a) Image guidance (b) Classifier guidance (c) DiffusionCLIP (d) Ours

Figure 1: **Manipulation approaches for diffusion models.** (a) Image guidance suffers ambiguity while controlling the generative process. (b) Classifier guidance requires an extra classifier, is hardly editable, degrades quality, or alters the content. (c) DiffusionCLIP requires fine-tuning the whole model. (d) Our method discovers a semantic latent space of a *frozen* diffusion model.

the reverse diffusion process: a latent vector from an original image embedded by an extra encoder. This latent vector contains the semantics to condition the process. However, it cannot use pretrained diffusion models because they cannot handle the external latent vectors. Inherently, the model should be trained from scratch.

In this paper, we propose an **asy**mmetric **r**everse **p**rocess (*Asyrp*) which discovers the semantic latent space of a *frozen* diffusion model where modification in the space synthesizes various attributes on input images. Our semantic latent space, named *h-space*, has practical properties for editing applications as follows. The same shift in this space results in the same attribute change in all images. Linear changes in this space lead to linear changes in attributes. The changes do not degrade the quality of the resulting images. The changes throughout the timesteps are almost identical to the desired attribute changes. Figure 1(d) illustrates some of these properties and § 5.3 provides detailed analyses. To the best of our knowledge, it is the first attempt to discover the semantic latent space in the frozen pretrained diffusion models. Spoiler alert: our semantic latent space is different from the intermediate latent variables in the diffusion process. Moreover, we introduce a principled design of the generative process for versatile editing and quality boosting by quantifiable measures: *editing strength* of an interval and *quality deficiency* at a timestep. Extensive experiments demonstrate that our method is generally applicable to various architectures (DDPM++, iDDPM, and ADM) and datasets (CelebA-HQ, AFHQ-dog, LSUN-church, LSUN-bedroom, and METFACES).

2 BACKGROUND

We briefly describe essential backgrounds. The rest of the related work is deferred to Appendix A.

2.1 DENOISING DIFFUSION PROBABILITY MODEL (DDPM)

DDPM is a latent variable model that learns a data distribution by denoising noisy images (Ho et al., 2020). The forward process diffuses the data samples through Gaussian transitions parameterized with a Markov process:

$$q\left(\boldsymbol{x}_t \mid \boldsymbol{x}_{t-1}\right)=\mathcal{N}\left(\boldsymbol{x}_t ; \sqrt{1-\beta_t} \boldsymbol{x}_{t-1}, \beta_t \mathbf{I}\right)=\mathcal{N}\left(\sqrt{\frac{\alpha_t}{\alpha_{t-1}}} \boldsymbol{x}_{t-1},\left(1-\frac{\alpha_t}{\alpha_{t-1}}\right) \boldsymbol{I}\right), \tag{1}$$

where $\{\beta_t\}_{t=1}^T$ is the variance schedule and $\alpha_t=\prod_{s=1}^t(1-\beta_s)$. Then the reverse process becomes $p_\theta\left(\boldsymbol{x}_{0:T}\right):=p\left(\boldsymbol{x}_T\right) \prod_{t=1}^T p_\theta\left(\boldsymbol{x}_{t-1} \mid \boldsymbol{x}_t\right)$, starting from $\boldsymbol{x}_T \sim \mathcal{N}(0, \mathbf{I})$ with noise predictor $\boldsymbol{\epsilon}_t^\theta$:

$$\boldsymbol{x}_{t-1}=\frac{1}{\sqrt{1-\beta_t}}\left(\boldsymbol{x}_t-\frac{\beta_t}{\sqrt{1-\alpha_t}} \boldsymbol{\epsilon}_t^\theta\left(\boldsymbol{x}_t\right)\right)+\sigma_t \boldsymbol{z}_t, \tag{2}$$

where $\boldsymbol{z}_t \sim \mathcal{N}(0, \mathbf{I})$ and σ_t^2 is a variance of the reverse process which is set to $\sigma_t^2=\beta_t$ by DDPM.

2.2 DENOISING DIFFUSION IMPLICIT MODEL (DDIM)

DDIM redefines Eq. (1) as $q_\sigma(\boldsymbol{x}_{t-1}|\boldsymbol{x}_t, \boldsymbol{x}_0) = \mathcal{N}(\sqrt{\alpha_{t-1}}\boldsymbol{x}_0 + \sqrt{1-\alpha_{t-1}-\sigma_t^2} \cdot \frac{\boldsymbol{x}_t - \sqrt{\alpha_t}\boldsymbol{x}_0}{\sqrt{1-\alpha_t}}, \sigma_t^2 \boldsymbol{I})$ which is a non-Markovian process (Song et al., 2020a). Accordingly, the reverse process becomes

$$\boldsymbol{x}_{t-1} = \sqrt{\alpha_{t-1}} \underbrace{\left(\frac{\boldsymbol{x}_t - \sqrt{1-\alpha_t}\boldsymbol{\epsilon}_t^\theta(\boldsymbol{x}_t)}{\sqrt{\alpha_t}} \right)}_{\text{"predicted } \boldsymbol{x}_0 \text{"}} + \underbrace{\sqrt{1-\alpha_{t-1}-\sigma_t^2} \cdot \boldsymbol{\epsilon}_t^\theta(\boldsymbol{x}_t)}_{\text{"direction pointing to } \boldsymbol{x}_t \text{"}} + \underbrace{\sigma_t \boldsymbol{z}_t}_{\text{random noise}}, \tag{3}$$

where $\sigma_t = \eta\sqrt{(1-\alpha_{t-1})/(1-\alpha_t)}\sqrt{1-\alpha_t/\alpha_{t-1}}$. When $\eta = 1$ for all t, it becomes DDPM. As $\eta = 0$, the process becomes deterministic and guarantees nearly perfect inversion.

2.3 IMAGE MANIPULATION WITH CLIP

CLIP learns multimodal embeddings with an image encoder E_I and a text encoder E_T whose similarity indicates semantic similarity between images and texts (Radford et al., 2021). Compared to directly minimizing the cosine distance between the edited image and the target description (Patashnik et al., 2021), directional loss with cosine distance achieves homogeneous editing without mode collapse (Gal et al., 2021):

$$\mathcal{L}_{\text{direction}}\left(\boldsymbol{x}^{\text{edit}}, y^{\text{target}}; \boldsymbol{x}^{\text{source}}, y^{\text{source}}\right) := 1 - \frac{\Delta I \cdot \Delta T}{\|\Delta I\| \|\Delta T\|}, \tag{4}$$

where $\Delta T = E_T\left(y^{\text{target}}\right) - E_T\left(y^{\text{source}}\right)$ and $\Delta I = E_I\left(\boldsymbol{x}^{\text{edit}}\right) - E_I\left(\boldsymbol{x}^{\text{source}}\right)$ for edited image $\boldsymbol{x}^{\text{edit}}$, target description y^{target}, original image $\boldsymbol{x}^{\text{source}}$, and source description y^{source}. We use the prompts 'smiling face' and 'face' as the target and source descriptions for facial attribute `smiling`.

3 DISCOVERING SEMANTIC LATENT SPACE IN DIFFUSION MODELS

This section explains why naive approaches do not work and proposes a new controllable reverse process. Then we describe the techniques for controlling the generative process. Throughout this paper, we use an abbreviated version of Eq. (3):

$$\boldsymbol{x}_{t-1} = \sqrt{\alpha_{t-1}}\, \mathbf{P}_t(\boldsymbol{\epsilon}_t^\theta(\boldsymbol{x}_t)) + \mathbf{D}_t(\boldsymbol{\epsilon}_t^\theta(\boldsymbol{x}_t)) + \sigma_t \boldsymbol{z}_t, \tag{5}$$

where $\mathbf{P}_t(\boldsymbol{\epsilon}_t^\theta(\boldsymbol{x}_t))$ denotes the predicted $\boldsymbol{x}_0$ and $\mathbf{D}_t(\boldsymbol{\epsilon}_t^\theta(\boldsymbol{x}_t))$ denotes the direction pointing to $\boldsymbol{x}_t$. We omit $\sigma_t \boldsymbol{z}_t$ for brevity, except when $\eta \neq 0$. We further abbreviate $\mathbf{P}_t(\boldsymbol{\epsilon}_t^\theta(\boldsymbol{x}_t))$ as $\mathbf{P}_t$ and $\mathbf{D}_t(\boldsymbol{\epsilon}_t^\theta(\boldsymbol{x}_t))$ as $\mathbf{D}_t$ when the context clearly specifies the arguments.

3.1 PROBLEM

We aim to allow semantic latent manipulation of images $\boldsymbol{x}_0$ generated from $\boldsymbol{x}_T$ given a *pretrained and frozen* diffusion model. The easiest idea to manipulate $\boldsymbol{x}_0$ is simply updating $\boldsymbol{x}_T$ to optimize the directional CLIP loss given text prompts with Eq. (4). However, it leads to distorted images or incorrect manipulation (Kim & Ye, 2021).

An alternative approach is to shift the noise $\boldsymbol{\epsilon}_t^\theta$ predicted by the network at each sampling step. However, it does not achieve manipulating $\boldsymbol{x}_0$ because the intermediate changes in $\mathbf{P}_t$ and $\mathbf{D}_t$ cancel out each other resulting in the same $p_\theta(\boldsymbol{x}_{0:T})$, similarly to destructive interference.

Theorem 1. *Let $\boldsymbol{\epsilon}_t^\theta$ be a predicted noise during the original reverse process at t and $\tilde{\boldsymbol{\epsilon}}_t^\theta$ be its shifted counterpart. Then, $\Delta\boldsymbol{x}_t = \tilde{\boldsymbol{x}}_{t-1} - \boldsymbol{x}_{t-1}$ is negligible where $\tilde{\boldsymbol{x}}_{t-1} = \sqrt{\alpha_{t-1}}\, \mathbf{P}_t(\tilde{\boldsymbol{\epsilon}}_t^\theta(\boldsymbol{x}_t)) + \mathbf{D}_t(\tilde{\boldsymbol{\epsilon}}_t^\theta(\boldsymbol{x}_t))$. I.e., the shifted terms of $\tilde{\boldsymbol{\epsilon}}_t^\theta$ in $\mathbf{P}_t$ and $\mathbf{D}_t$ destruct each other in the reverse process.*

Appendix C proves above theorem. Figure 13(a-b) shows that $\tilde{\boldsymbol{x}}_0$ is almost identical to $\boldsymbol{x}_0$.

3.2 ASYMMETRIC REVERSE PROCESS

In order to break the interference, we propose a new controllable reverse process with asymmetry:

$$\boldsymbol{x}_{t-1} = \sqrt{\alpha_{t-1}}\, \mathbf{P}_t(\tilde{\boldsymbol{\epsilon}}_t^\theta(\boldsymbol{x}_t)) + \mathbf{D}_t(\boldsymbol{\epsilon}_t^\theta(\boldsymbol{x}_t)), \tag{6}$$

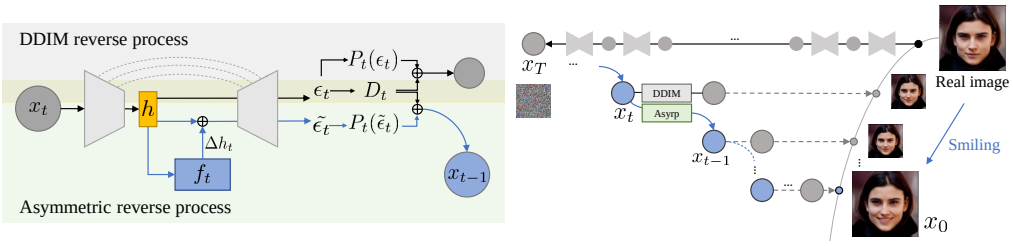

Figure 2: **Generative process of Asyrp.** The green box on the left illustrates Asyrp which only alters $\mathbf{P}_t$ while preserving $\mathbf{D}_t$ shared by DDIM. The right describes that Asyrp modifies the original reverse process toward the target attribute reflecting the change in *h-space*.

i.e., we modify only $\mathbf{P}_t$ by shifting $\boldsymbol{\epsilon}_t^\theta$ to $\tilde{\boldsymbol{\epsilon}}_t^\theta$ while preserving $\mathbf{D}_t$. Intuitively, it modifies the original reverse process according to $\Delta\boldsymbol{\epsilon}_t = \tilde{\boldsymbol{\epsilon}}_t^\theta - \boldsymbol{\epsilon}_t^\theta$ while it does not alter the direction toward $\boldsymbol{x}_t$ so that $\boldsymbol{x}_{t-1}$ follows the original flow $\mathbf{D}_t$ at each sampling step. Figure 2 illustrates the above intuition.

As in Avrahami et al. (2022), we use the modified $\mathbf{P}_t^{\text{edit}}$ and the original $\mathbf{P}_t^{\text{source}}$ as visual inputs for the directional CLIP loss in Eq. (4), and regularize the difference between the modified $\boldsymbol{x}_t^{\text{edit}}$ and the original $\boldsymbol{x}_t^{\text{source}}$. We find $\Delta\boldsymbol{\epsilon} = \arg\min_{\Delta\boldsymbol{\epsilon}} \mathbb{E}_t \mathcal{L}^{(t)}$ where

$$\mathcal{L}^{(t)} = \lambda_{\text{CLIP}} \mathcal{L}_{\text{direction}} \left(\mathbf{P}_t^{\text{edit}}, y^{\text{ref}}; \mathbf{P}_t^{\text{source}}, y^{\text{source}}\right) + \lambda_{\text{recon}} \left|\boldsymbol{x}_t^{\text{edit}} - \boldsymbol{x}_t^{\text{source}}\right| \tag{7}$$

Although $\Delta\boldsymbol{\epsilon}$ indeed renders the attribute in the $\boldsymbol{x}_0^{\text{edit}}$, $\boldsymbol{\epsilon}$-space lacks the necessary properties of the semantic latent space in diffusion models that will be described in the following.

3.3 *h-space*

Note that $\boldsymbol{\epsilon}_t^\theta$ is implemented as U-Net in all state-of-the-art diffusion models. We choose its bottleneck, the deepest feature maps $\boldsymbol{h}_t$, to control $\boldsymbol{\epsilon}_t^\theta$. By design, $\boldsymbol{h}_t$ has smaller spatial resolutions and high-level semantics than $\boldsymbol{\epsilon}_t^\theta$. Accordingly, the sampling equation becomes

$$\boldsymbol{x}_{t-1} = \sqrt{\alpha_{t-1}}\, \mathbf{P}_t(\boldsymbol{\epsilon}_t^\theta(\boldsymbol{x}_t|\Delta\boldsymbol{h}_t)) + \mathbf{D}_t(\boldsymbol{\epsilon}_t^\theta(\boldsymbol{x}_t)) + \sigma_t \boldsymbol{z}_t, \tag{8}$$

where $\boldsymbol{\epsilon}_t^\theta(\boldsymbol{x}_t|\Delta\boldsymbol{h}_t)$ adds $\Delta\boldsymbol{h}_t$ to the original feature maps $\boldsymbol{h}_t$. The $\Delta\boldsymbol{h}_t$ minimizing the same loss in Eq. (7) with $\mathbf{P}_t(\boldsymbol{\epsilon}_t^\theta(\boldsymbol{x}_t|\Delta\boldsymbol{h}_t))$ instead of $\mathbf{P}_t(\tilde{\boldsymbol{\epsilon}}_t^\theta(\boldsymbol{x}_t))$ successfully manipulates the attributes.

We observe that *h-space* in Asyrp has the following properties that others do not have.

- The same $\Delta\boldsymbol{h}$ leads to the same effect on different samples.
- Linearly scaling $\Delta\boldsymbol{h}$ controls the magnitude of attribute change, even with negative scales.
- Adding multiple $\Delta\boldsymbol{h}$ manipulates the corresponding multiple attributes simultaneously.
- $\Delta\boldsymbol{h}$ preserves the quality of the resulting images without degradation.
- $\Delta\boldsymbol{h}_t$ is roughly consistent across different timesteps t.

The above properties are demonstrated thoroughly in § 5.3. Appendix D.3 provides details of *h-space* and results with suboptimal choices.

3.4 Implicit neural directions

Although $\Delta\boldsymbol{h}$ succeeds in manipulating images, directly optimizing $\Delta\boldsymbol{h}_t$ on multiple timesteps requires many iterations of training with a carefully chosen learning rate and its scheduling. Instead, we define an implicit function $\boldsymbol{f}_t(\boldsymbol{h}_t)$ which produces $\Delta\boldsymbol{h}_t$ for given $\boldsymbol{h}_t$ and t. $\boldsymbol{f}_t$ is implemented as a small neural network with two 1×1 convolutions concatenating timestep t. See Appendix E for the details. Accordingly, we optimize the same loss in Eq. (7) with $\mathbf{P}_t^{\text{edit}} = \mathbf{P}_t(\boldsymbol{\epsilon}_t^\theta(\boldsymbol{x}_t|\boldsymbol{f}_t))$.

Learning $\boldsymbol{f}_t$ is more robust to learning rate settings and converges faster than learning every $\Delta\boldsymbol{h}_t$. In addition, as $\boldsymbol{f}_t$ learns an implicit function for given timesteps and bottleneck features, it generalizes

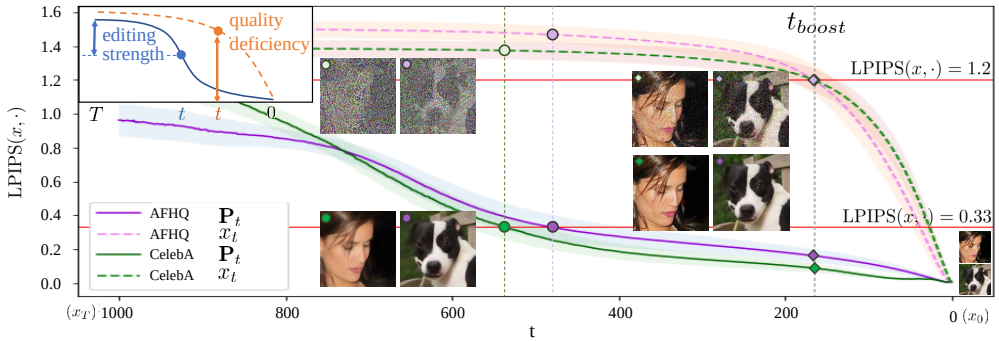

Figure 3: **Intuition for choosing the intervals for editing and quality boosting.** We choose the intervals by quantifying three measures (top left inset). The editing strength of an interval $[T, t]$ measures its perceptual difference from T until t. We set $[T, t]$ to the interval with the smallest editing strength that synthesizes $\mathbf{P}_t$ close to $\boldsymbol{x}$, i.e., $\text{LPIPS}(\boldsymbol{x}, \mathbf{P}_t) = 0.33$. Editing flexibility of an interval $[t, 0]$ measures the potential amount of changes after t. Quality deficiency at t measures the amount of noise in $\boldsymbol{x}_t$. We set $[t, 0]$ to handle large quality deficiency (i.e., $\text{LPIPS}(\boldsymbol{x}, \boldsymbol{x}_t) = 1.2$) with small editing flexibility.

to unseen timesteps and bottleneck features. The generalization allows us to borrow the accelerated training scheme of DDIM defined on a subsequence $\{\boldsymbol{x}_{\tau_i}\}_{\forall i \in [1,S]}$ where $\{\tau_i\}$ is a subsequence of $[1, ..., T]$ and $S < T$. Then, we can use the generative process with a custom subsequence $\{\tilde{\tau}_i\}$ with length $\tilde{S} < T$ through normalization: $\Delta\tilde{\boldsymbol{h}}_{\tilde{\tau}} = \boldsymbol{f}_{\tilde{\tau}}(\boldsymbol{h}_{\tilde{\tau}})S/\tilde{S}$. It preserves the amount of $\sum \Delta\boldsymbol{h}_t$, $\Delta\tilde{\boldsymbol{h}}_{\tilde{\tau}}\tilde{S} = \Delta\boldsymbol{h}_t S$. Therefore, we can use $\boldsymbol{f}_t$ trained on any subsequence for any length of the generative process. See Appendix F for details. We use $\boldsymbol{f}_t$ to get $\Delta\boldsymbol{h}_t$ for all experiments except Figure 6.

4 Generative Process Design

This section describes the entire editing process, which consists of three phases: editing with Asyrp, traditional denoising, and quality boosting. We design formulas to determine the length of each phase with quantifiable measures.

4.1 Editing Process with Asyrp

Diffusion models generate the high-level context in the early stage and imperceptible fine details in the later stage (Choi et al., 2022). Likewise, we modify the generative process in the early stage to achieve semantic changes. We refer to the early stage as the editing interval $[T, t_{\text{edit}}]$.

$\text{LPIPS}(\boldsymbol{x}, \mathbf{P}_T)$ and $\text{LPIPS}(\boldsymbol{x}, \mathbf{P}_t)$ calculate the perceptual distance between the original image and the predicted image at time steps T and t, respectively. Intuitively, the high-level content is already determined by the predicted terms at the respective timesteps and LPIPS measures the remaining component to be edited through the remaining reverse process. Consequently, we define *editing strength* of an interval $[T, t]$:

$$\xi_t = \text{LPIPS}(\boldsymbol{x}, \mathbf{P}_T) - \text{LPIPS}(\boldsymbol{x}, \mathbf{P}_t)$$

indicating the perceptual change from timestep T to t in the original generative process. Figure 3 illustrates $\text{LPIPS}(\boldsymbol{x}, \cdot)$ for $\mathbf{P}_t$ and $\boldsymbol{x}_t$ with examples and the inset depicts editing strength. The shorter editing interval has the lower ξ_t, and the longer editing interval brings more changes to the resulting images. We seek the shortest editing interval which will bring enough distinguishable changes in the images in general. We empirically find that t_{edit} with $\text{LPIPS}(\boldsymbol{x}, \mathbf{P}_{t_{\text{edit}}}) = 0.33$ builds the shortest editing interval with enough editing strength as $\mathbf{P}_{t_{\text{edit}}}$ has nearly all visual attributes in $\boldsymbol{x}$.

However, some attributes require more visual changes than others, e.g., `pixar` > `smile`. For such attributes, we increase the editing strength ξ_t by $\delta = 0.33d(E_T(y_{\text{source}}), E_T(y_{\text{target}}))$ where

$E_T(\cdot)$ produces CLIP text embedding, $y_{(\cdot)}$ denotes the descriptions, and $d(\cdot,\cdot)$ computes the cosine distance between the arguments. Choosing t_{edit} with $\text{LPIPS}(\boldsymbol{x}, \mathbf{P}_{t_{\text{edit}}}) = 0.33 - \delta$ expands the editing interval to a suitable length. It consistently produces good results in various settings. The supporting experiments are shown in Appendix G.

4.2 Quality boosting with stochastic noise injection

Although DDIM achieves nearly perfect inversion by removing stochasticity ($\eta = 0$), Karras et al. (2022) demonstrate that stochasticity improves image quality. Likewise, we inject stochastic noise in the boosting interval $[t_{\text{boost}}, 0]$.

Though the longer boosting interval would achieve higher quality, boosting over excessively long intervals would modify the content. Hence, we want to determine the shortest interval that shows enough quality boosting to guarantee minimal change in the content. We consider the noise in the image as the capacity for the quality boosting and define *quality deficiency* at t: $\gamma_t = \text{LPIPS}(\boldsymbol{x}, \boldsymbol{x}_t)$ indicating the amount of noise in $\boldsymbol{x}_t$ compared to the original image. We use $\boldsymbol{x}_t$ instead of $\mathbf{P}_t$ because we consider the actual image rather than the semantics. Figure 3 inset depicts editing flexibility and quality deficiency. We empirically find that t_{boost} with $\gamma_{t_{\text{boost}}} = 1.2$ achieves quality boosting with minimal content change. We confirmed that the editing strength of the intervals $[t_{\text{boost}}, 0]$ is guaranteed to be less than 0.25. In Figure 3, after t_{boost}, $\text{LPIPS}(\boldsymbol{x}, \boldsymbol{x}_t)$ sharply drops in the original generative process while $\text{LPIPS}(\boldsymbol{x}, \mathbf{P}_t)$ changes little. Note that most of the quality degradation of the resulting images is caused by DDIM reverse process, not by Asyrp. We use this quality boosting for all experiments except ablation in Appendix H.

4.3 Overall process of image editing

Using t_{edit} and t_{boost} determined by the above formulas, we modify the generative process of DDIM with

$$p_\theta^{(t)}(\boldsymbol{x}_{t-1} \mid \boldsymbol{x}_t) = \begin{cases} \mathcal{N}\left(\sqrt{\alpha_{t-1}}\,\mathbf{P}_t(\boldsymbol{\epsilon}_t^\theta(\boldsymbol{x}_t|\boldsymbol{f}_t)) + \mathbf{D}_t, \sigma_t^2 \boldsymbol{I}\right),\ \eta = 0 & \text{if } T \geq t \geq t_{\text{edit}} \\ \mathcal{N}\left(\sqrt{\alpha_{t-1}}\,\mathbf{P}_t(\boldsymbol{\epsilon}_t^\theta(\boldsymbol{x}_t)) + \mathbf{D}_t, \sigma_t^2 \boldsymbol{I}\right),\ \eta = 0 & \text{if } t_{\text{edit}} > t \geq t_{\text{boost}} \\ \mathcal{N}\left(\sqrt{\alpha_{t-1}}\,\mathbf{P}_t(\boldsymbol{\epsilon}_t^\theta(\boldsymbol{x}_t)) + \mathbf{D}_t, \sigma_t^2 \boldsymbol{I}\right),\ \eta = 1 & \text{if } t_{\text{boost}} > t \end{cases} \tag{9}$$

The visual overview and comprehensive algorithms of the entire process are in Appendix I.

5 Experiments

In this section, we show the effectiveness of semantic latent editing in *h-space* with Asyrp on various attributes, datasets and architectures in § 5.1. Moreover, we provide quantitative results including user study in § 5.2. Lastly, we provide detailed analyses for the properties of the semantic latent space on *h-space* and alternatives in § 5.3.

Implementation details. We implement our method on various settings: CelebA-HQ (Karras et al., 2018) and LSUN-bedroom/-church (Yu et al., 2015) on DDPM++ (Song et al., 2020b) (Meng et al., 2021); AFHQ-dog (Choi et al., 2020) on iDDPM (Nichol & Dhariwal, 2021); and MetFaces (Karras et al., 2020) on ADM with P2-weighting (Dhariwal & Nichol, 2021) (Choi et al., 2022). Please note that all models are official pretrained checkpoints and are kept frozen. Detailed settings including the coefficients for λ_{CLIP} and λ_{recon}, and source/target descriptions can be found in Appendix J.1. We train $\boldsymbol{f}_t$ with $S = 40$ for 1 epoch using 1000 samples. The real samples are randomly chosen from each dataset for in-domain-like attributes. For out-of-domain-like attributes, we randomly draw 1,000 latent variables $\boldsymbol{x}_T \sim \mathcal{N}(0, \boldsymbol{I})$. Details are described in Appendix J.2. Training takes about 20 minutes with three RTX 3090 GPUs. All the images in the figures are not used for training. We set $\tilde{S} = 1,000$ for inference. The code is attached to the supplementary materials and will be available online with publication.

5.1 Versatility of *h-space* with Asyrp

Figure 4 shows the effectiveness of our method on various datasets and any existing U-Net based architectures. Our method can synthesize the attributes that are not even included in the training

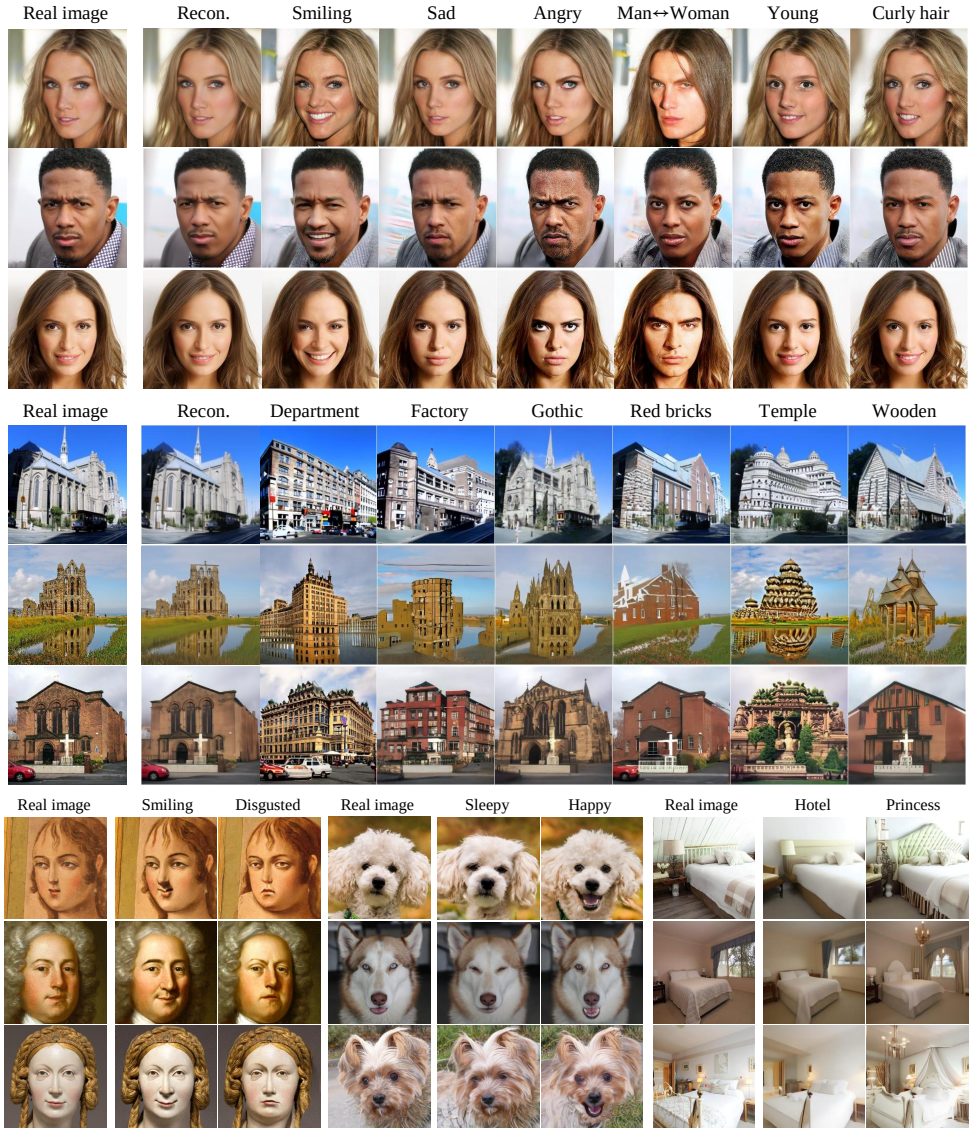

Figure 4: **Editing results of Asyrp on various datasets.** We conduct experiments on CelebA-HQ, LSUN-church, METFACES, AFHQ-dog, and LSUN-bedroom.

Figure 5: **Editing results of Asyrp for unseen domains in CelebA-HQ dataset.**

dataset, such as church → {`department`, `factory`, and `temple`}. Even for dogs, our method synthesizes `smiling` Poodle and Yorkshire, the species that barely smile in the dataset. Figure 5 provides results for changing human faces to different identities, painting styles, and ancient primates. More result can be found in Appendix N. Versatility of our method is surprising because we do *not* alter the models but only shift the bottleneck feature maps in *h-space* with Asyrp during inference.

	CelebA-HQ in-domain			CelebA-HQ unseen-domain			LSUN-church			
	quality	attribute	overall	quality	attribute	overall	quality	attribute	diversity	overall
Asyrp (ours)	**98.36%**	**88.13%**	**94.92%**	**71.56%**	**59.84%**	**63.13%**	**73.19%**	**71.81%**	**87.50%**	**76.81%**
DiffusionCLIP	1.64%	11.88%	5.08%	28.44%	40.16%	36.88%	26.81%	28.19%	12.50%	23.19%

Table 1: **User study.** with 80 participants. The setting of the user study is described in § K.1

(a) Result of optimization (b) Result of adaptation to other images

Figure 6: **Optimization on *h-space* and *ϵ-space*.** (a) Optimizing $\Delta \boldsymbol{h}_t$ for a sample with `smiling` results in natural editing while the change due to optimizing $\Delta \boldsymbol{\epsilon}_t$ is relatively small. (b) Applying $\Delta \boldsymbol{h}_t$ from (a) to other samples yields the same attribute change while $\Delta \boldsymbol{\epsilon}_t$ distorts the images. The result of $\Delta \boldsymbol{\epsilon}_t$ at the end is the best sample we could find.

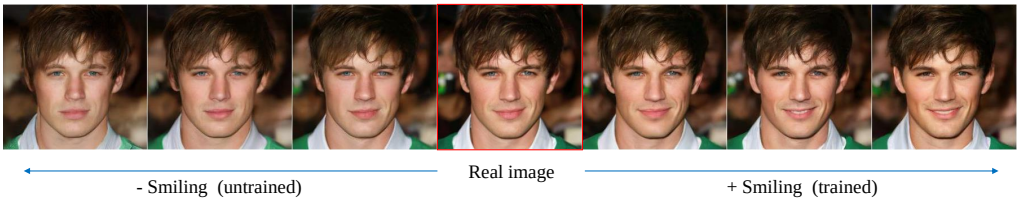

Figure 7: **Linearity property of *h-space*.** Linear interpolation and extrapolation on *h-space* lead to gradual changes even to the unseen intensity and directions. Right side shows the interpolation results by positive scaling of $\Delta h_t^{\texttt{smiling}}$. Left side shows the extrapolation results by negative scaling of $\Delta h_t^{smiling}$. Note that we did not train $\boldsymbol{f}_t$ for the negative direction.

5.2 Quantitative comparison

Considering that our method can be combined with various diffusion models *without* finetuning, we do not find such a versatile competitor. Nonetheless, we compare Asyrp against DiffusionCLIP using the official code that edits the real images by finetuning the whole model. We asked 80 participants to choose the images with better quality, natural attribute change, and overall preference for given total of 40 sets of original images, ours, and DiffusionCLIP. Table 1 shows that Asyrp outperforms DiffusionCLIP in the all perspectives including the attributes unseen in the training dataset. We list the settings for fair comparison including the questions and example images in Appendix K.1. See § K.2 for more evaluation metrics: segmentation consistency (SC) and directional CLIP similarity(S_{dir}).

5.3 Analysis on *h-space*

We provide detailed analyses to validate the properties of semantic latent space for diffusion models: homogeneity, linearity, robustness, and consistency across timesteps.

Homogeneity. Figure 6 illustrates homogeneity of *h-space* compared to $\boldsymbol{\epsilon}$-space. One $\Delta \boldsymbol{h}_t$ optimized for an image results in the same attribute change to other input images. On the other hand, one $\Delta \boldsymbol{\epsilon}_t$ optimized for an image distorts other input images. In Figure 10, applying $\Delta \boldsymbol{h}_t^{\text{mean}} = \frac{1}{N} \sum \Delta \boldsymbol{h}_t^i$ produces almost identical results where i indicates indices of $N = 20$ random samples.

Linearity. In Figure 7, we observe that linearly scaling a $\Delta \boldsymbol{h}$ reflects the amount of change in the visual attributes. Surprisingly, it generalizes to negative scales that are not seen during training. Moreover, Figure 8 shows that combinations of different $\Delta \boldsymbol{h}$'s yield their combined semantic changes in the resulting images. Appendix N.1 provides mixed interpolation between multiple attributes.

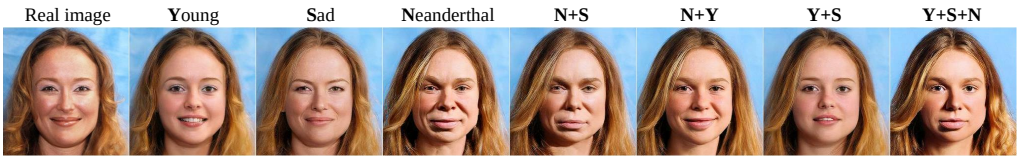

Figure 8: **Linear combination.** Combining multiple $\Delta \boldsymbol{h}$s leads to combined attribute changes.

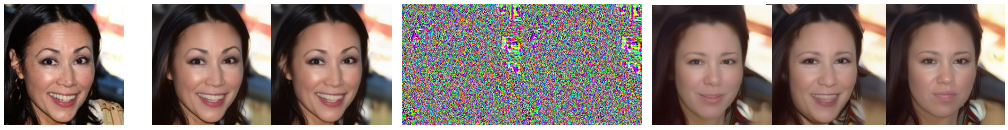

Figure 9: **Ramdom manipulation on *h-space* and ϵ-space.** (a) Adding random noise with magnitude of $\Delta \boldsymbol{h}_t^{\texttt{smiling}}$ and random direction in *h-space* leads to realistic images with small changes. (b) Adding random noise with magnitude of $\Delta \boldsymbol{\epsilon}_t^{\texttt{smiling}}$ and random direction in $\boldsymbol{\epsilon}$-space leads to severely distorted images. (c) Adding random noises with tripled magnitude produce diverse visual changes in realistic images.

Figure 10: **Consistency on *h-space*.** Results of $\Delta \boldsymbol{h}_t$, $\Delta \boldsymbol{h}_t^{\text{mean}}$ and $\Delta \boldsymbol{h}^{\text{global}}$ are almost identical for in-domain samples. However, we choose $\Delta \boldsymbol{h}_t$ over others to prevent unexpected small difference in the unseen domain. We provide more results in § L.1.

Robustness. Figure 9 compares the effect of adding random noise in *h-space* and $\boldsymbol{\epsilon}$-space. The random noises are chosen to be the vectors with random directions and magnitude of the example $\Delta \boldsymbol{h}_t$ and $\Delta \boldsymbol{\epsilon}_t$ in Figure 6 on each space. Perturbation in *h-space* leads to realistic images with a minimal difference or some semantic changes. On the contrary, perturbation in $\boldsymbol{\epsilon}$-space severely distorts the resulting images. See Appendix D.2 for more analyses.

Rough consistency across timesteps. Recall that $\Delta \boldsymbol{h}_t$ for all samples are homogeneous and replacing them by their mean $\Delta \boldsymbol{h}_t^{\text{mean}}$ yields similar results. Interestingly, in Figure 10, we observe that adding a time-invariant $\Delta \boldsymbol{h}^{\text{global}} = \frac{1}{T_e} \sum_t \Delta \boldsymbol{h}_t^{\text{mean}}$ instead of $\Delta \boldsymbol{h}_t$ also yields similar results where T_e denotes the length of the editing interval $[T, t_{\text{edit}}]$. Though we use $\Delta \boldsymbol{h}_t$ to deliver the best quality and manipulation, using $\Delta \boldsymbol{h}_t^{\text{mean}}$ or even $\Delta \boldsymbol{h}^{\text{global}}$ with some compromise would be worth trying for simplicity. We report more detail about mean and global direction in Appendix L.1.

6 Conclusion

We proposed a new generative process, Asyrp, which facilitates image editing in a semantic latent space *h-space* for pretrained diffusion models. *h-space* has nice properties as in the latent space of GANs: homogeneity, linearity, robustness, and consistency across timesteps. The full editing process is designed to achieve versatile editing and high quality according to a quantitative measure of editing strength and quality deficiency at timesteps. We hope that our approach and detailed analyses help cultivate a new paradigm of image editing in the semantic latent space of diffusion models. Combining previous finetuning or guidance techniques would be an interesting research direction.

REFERENCES

Omri Avrahami, Dani Lischinski, and Ohad Fried. Blended diffusion for text-driven editing of natural images. In *Proceedings of the IEEE/CVF Conference on Computer Vision and Pattern Recognition*, pp. 18208–18218, 2022.

Hila Chefer, Sagie Benaim, Roni Paiss, and Lior Wolf. Image-based clip-guided essence transfer. *arXiv preprint arXiv:2110.12427*, 2021.

Jooyoung Choi, Sungwon Kim, Yonghyun Jeong, Youngjune Gwon, and Sungroh Yoon. Ilvr: Conditioning method for denoising diffusion probabilistic models. *arXiv preprint arXiv:2108.02938*, 2021.

Jooyoung Choi, Jungbeom Lee, Chaehun Shin, Sungwon Kim, Hyunwoo Kim, and Sungroh Yoon. Perception prioritized training of diffusion models. In *Proceedings of the IEEE/CVF Conference on Computer Vision and Pattern Recognition*, pp. 11472–11481, 2022.

Yunjey Choi, Youngjung Uh, Jaejun Yoo, and Jung-Woo Ha. Stargan v2: Diverse image synthesis for multiple domains. In *Proceedings of the IEEE/CVF conference on computer vision and pattern recognition*, pp. 8188–8197, 2020.

Ning Dai, Jianze Liang, Xipeng Qiu, and Xuanjing Huang. Style transformer: Unpaired text style transfer without disentangled latent representation. *arXiv preprint arXiv:1905.05621*, 2019.

Prafulla Dhariwal and Alexander Nichol. Diffusion models beat gans on image synthesis. *Advances in Neural Information Processing Systems*, 34:8780–8794, 2021.

Rinon Gal, Or Patashnik, Haggai Maron, Gal Chechik, and Daniel Cohen-Or. Stylegan-nada: Clip-guided domain adaptation of image generators. *arXiv preprint arXiv:2108.00946*, 2021.

Ian Goodfellow, Jean Pouget-Abadie, Mehdi Mirza, Bing Xu, David Warde-Farley, Sherjil Ozair, Aaron Courville, and Yoshua Bengio. Generative adversarial networks. *Communications of the ACM*, 63(11):139–144, 2020.

Erik Härkönen, Aaron Hertzmann, Jaakko Lehtinen, and Sylvain Paris. Ganspace: Discovering interpretable gan controls. *Advances in Neural Information Processing Systems*, 33:9841–9850, 2020.

Jonathan Ho, Ajay Jain, and Pieter Abbeel. Denoising diffusion probabilistic models. *Advances in Neural Information Processing Systems*, 33:6840–6851, 2020.

Tero Karras, Timo Aila, Samuli Laine, and Jaakko Lehtinen. Progressive growing of gans for improved quality, stability, and variation. In *International Conference on Learning Representations*, 2018.

Tero Karras, Miika Aittala, Janne Hellsten, Samuli Laine, Jaakko Lehtinen, and Timo Aila. Training generative adversarial networks with limited data. *Advances in Neural Information Processing Systems*, 33:12104–12114, 2020.

Tero Karras, Miika Aittala, Timo Aila, and Samuli Laine. Elucidating the design space of diffusion-based generative models. *arXiv preprint arXiv:2206.00364*, 2022.

Gwanghyun Kim and Jong Chul Ye. Diffusionclip: Text-guided image manipulation using diffusion models. 2021.

Diederik P Kingma and Max Welling. Auto-encoding variational bayes. *arXiv preprint arXiv:1312.6114*, 2013.

Cheng-Han Lee, Ziwei Liu, Lingyun Wu, and Ping Luo. Maskgan: Towards diverse and interactive facial image manipulation. In *Proceedings of the IEEE/CVF Conference on Computer Vision and Pattern Recognition*, pp. 5549–5558, 2020.

Huan Ling, Karsten Kreis, Daiqing Li, Seung Wook Kim, Antonio Torralba, and Sanja Fidler. Editgan: High-precision semantic image editing. *Advances in Neural Information Processing Systems*, 34:16331–16345, 2021.

Xihui Liu, Dong Huk Park, Samaneh Azadi, Gong Zhang, Arman Chopikyan, Yuxiao Hu, Humphrey Shi, Anna Rohrbach, and Trevor Darrell. More control for free! image synthesis with semantic diffusion guidance. *arXiv preprint arXiv:2112.05744*, 2021.

Ziwei Liu, Ping Luo, Xiaogang Wang, and Xiaoou Tang. Deep learning face attributes in the wild. In *Proceedings of International Conference on Computer Vision (ICCV)*, December 2015.

Andreas Lugmayr, Martin Danelljan, Andres Romero, Fisher Yu, Radu Timofte, and Luc Van Gool. Repaint: Inpainting using denoising diffusion probabilistic models. In *Proceedings of the IEEE/CVF Conference on Computer Vision and Pattern Recognition*, pp. 11461–11471, 2022.

Chenlin Meng, Yang Song, Jiaming Song, Jiajun Wu, Jun-Yan Zhu, and Stefano Ermon. Sdedit: Image synthesis and editing with stochastic differential equations. *arXiv preprint arXiv:2108.01073*, 2021.

Alex Nichol, Prafulla Dhariwal, Aditya Ramesh, Pranav Shyam, Pamela Mishkin, Bob McGrew, Ilya Sutskever, and Mark Chen. Glide: Towards photorealistic image generation and editing with text-guided diffusion models. *arXiv preprint arXiv:2112.10741*, 2021.

Alexander Quinn Nichol and Prafulla Dhariwal. Improved denoising diffusion probabilistic models. In *International Conference on Machine Learning*, pp. 8162–8171. PMLR, 2021.

Or Patashnik, Zongze Wu, Eli Shechtman, Daniel Cohen-Or, and Dani Lischinski. Styleclip: Text-driven manipulation of stylegan imagery. In *Proceedings of the IEEE/CVF International Conference on Computer Vision*, pp. 2085–2094, 2021.

Konpat Preechakul, Nattanat Chatthee, Suttisak Wizadwongsa, and Supasorn Suwajanakorn. Diffusion autoencoders: Toward a meaningful and decodable representation. In *Proceedings of the IEEE/CVF Conference on Computer Vision and Pattern Recognition*, pp. 10619–10629, 2022.

Alec Radford, Jong Wook Kim, Chris Hallacy, Aditya Ramesh, Gabriel Goh, Sandhini Agarwal, Girish Sastry, Amanda Askell, Pamela Mishkin, Jack Clark, et al. Learning transferable visual models from natural language supervision. In *International Conference on Machine Learning*, pp. 8748–8763. PMLR, 2021.

Robin Rombach, Andreas Blattmann, Dominik Lorenz, Patrick Esser, and Björn Ommer. High-resolution image synthesis with latent diffusion models. In *Proceedings of the IEEE/CVF Conference on Computer Vision and Pattern Recognition*, pp. 10684–10695, 2022.

David E Rumelhart, Geoffrey E Hinton, and Ronald J Williams. Learning internal representations by error propagation. Technical report, California Univ San Diego La Jolla Inst for Cognitive Science, 1985.

Vikash Sehwag, Caner Hazirbas, Albert Gordo, Firat Ozgenel, and Cristian Canton. Generating high fidelity data from low-density regions using diffusion models. In *Proceedings of the IEEE/CVF Conference on Computer Vision and Pattern Recognition*, pp. 11492–11501, 2022.

Yujun Shen, Ceyuan Yang, Xiaoou Tang, and Bolei Zhou. Interfacegan: Interpreting the disentangled face representation learned by gans. *IEEE transactions on pattern analysis and machine intelligence*, 2020.

Jascha Sohl-Dickstein, Eric Weiss, Niru Maheswaranathan, and Surya Ganguli. Deep unsupervised learning using nonequilibrium thermodynamics. In *International Conference on Machine Learning*, pp. 2256–2265. PMLR, 2015.

Jiaming Song, Chenlin Meng, and Stefano Ermon. Denoising diffusion implicit models. *arXiv preprint arXiv:2010.02502*, 2020a.

Yang Song, Jascha Sohl-Dickstein, Diederik P Kingma, Abhishek Kumar, Stefano Ermon, and Ben Poole. Score-based generative modeling through stochastic differential equations. *arXiv preprint arXiv:2011.13456*, 2020b.

Arash Vahdat, Karsten Kreis, and Jan Kautz. Score-based generative modeling in latent space. *Advances in Neural Information Processing Systems*, 34:11287–11302, 2021.

Daniel Watson, William Chan, Jonathan Ho, and Mohammad Norouzi. Learning fast samplers for diffusion models by differentiating through sample quality. In *International Conference on Learning Representations*, 2022. URL https://openreview.net/forum?id=VFBjuF8HEp.

Zipeng Xu, Tianwei Lin, Hao Tang, Fu Li, Dongliang He, Nicu Sebe, Radu Timofte, Luc Van Gool, and Errui Ding. Predict, prevent, and evaluate: Disentangled text-driven image manipulation empowered by pre-trained vision-language model. In *Proceedings of the IEEE/CVF Conference on Computer Vision and Pattern Recognition*, pp. 18229–18238, 2022.

Changqian Yu, Jingbo Wang, Chao Peng, Changxin Gao, Gang Yu, and Nong Sang. Bisenet: Bilateral segmentation network for real-time semantic segmentation. In *Proceedings of the European conference on computer vision (ECCV)*, pp. 325–341, 2018.

Fisher Yu, Ari Seff, Yinda Zhang, Shuran Song, Thomas Funkhouser, and Jianxiong Xiao. Lsun: Construction of a large-scale image dataset using deep learning with humans in the loop. *arXiv preprint arXiv:1506.03365*, 2015.

Oğuz Kaan Yüksel, Enis Simsar, Ezgi Gülperi Er, and Pinar Yanardag. Latentclr: A contrastive learning approach for unsupervised discovery of interpretable directions. In *Proceedings of the IEEE/CVF International Conference on Computer Vision*, pp. 14263–14272, 2021.

Bolei Zhou, Hang Zhao, Xavier Puig, Sanja Fidler, Adela Barriuso, and Antonio Torralba. Scene parsing through ade20k dataset. In *Proceedings of the IEEE conference on computer vision and pattern recognition*, pp. 633–641, 2017.

Bolei Zhou, Hang Zhao, Xavier Puig, Tete Xiao, Sanja Fidler, Adela Barriuso, and Antonio Torralba. Semantic understanding of scenes through the ade20k dataset. *International Journal of Computer Vision*, 127(3):302–321, 2019.

Appendix

Table of Contents

A Related work **14**

B More discussion **15**

C Proof of Theorem 1 **15**

D Additional supports for *h-space* with Asyrp **16**
D.1 Random perturbation on ϵ-*space* without Asyrp 16
D.2 Robustness and semantics in *h-space* and ϵ-*space* with Asyrp 17
D.3 Choice of *h-space* in U-Net 18

E Implicit neural directions **18**

F Quality improvements by non-accelerated sampling with scaled Δh_t **19**

G Editing strength and editing flexibility **20**
G.1 Editing strength and t_{edit} 20
G.2 Editing flexibility and t_{boost} 21

H Quality boosting **22**

I Algorithm **22**

J Training details **22**
J.1 Loss coefficients 22
J.2 Training with random sampling instead of the training datasets 22

K Evaluation **25**
K.1 User study 25
K.2 Segmentation consistency and directional CLIP similarity 26

L Directions **29**
L.1 Global direction 29
L.2 Compare three methods 31

M Random sampling **32**

N More samples **32**
N.1 Multi-interpolation 32
N.2 More results on all datasets 32

Figure 11: **Editing dog to smile.** We provide high-resolution results of editing real images in the teaser and more.

A Related work

After Sohl-Dickstein et al. (2015), denoising diffusion probabilistic models (DDPMs) provide a universal approach for generative modeling (Ho et al., 2020). On the other hand, Song et al. (2020b) suggests score-based model and unifies SDEs incorporating diffusion models with score-based models. Subsequent works renovate diffusion models by focusing on architectures, scheduling, weighting, and fast sampling (Nichol & Dhariwal (2021), Karras et al. (2022), Choi et al. (2022), Song et al. (2020a), Watson et al. (2022)). They mainly consider random generation rather than controlled generation.

In the mean time, Dhariwal & Nichol (2021) introduces classifier guidance not only improving quality of images but also retrieving specific class of images. Since it can apply any guidance, its variants have emerged (Sehwag et al. (2022), Avrahami et al. (2022), Liu et al. (2021), Nichol et al. (2021)). However it requires a noise-dependent classifier (or any off-the-shelf models) and additional cost to compute gradients for the guidance during its sampling process. The other works try to control the generative process using image-space guidance (Choi et al. (2021), Meng et al. (2021), Lugmayr et al. (2022), Avrahami et al. (2022)). They manipulate resulting images by matching noisy images with target images during the reverse process. Still, it is hard to expect delicate control of the reverse process from the image guidance. Furthermore, Preechakul et al. (2022) introduces an extra encoder which encodes the semantic features of a real image in order to condition the generative process. Although the semantics allow one to control diffusion models, it requires additional training from scratch with the encoder and inherently can not use the other pretrained diffusion models.

For controllability, Rombach et al. (2022) and Vahdat et al. (2021) apply another approach which adapts VAE (Kingma & Welling, 2013) and autoencoder (Rumelhart et al., 1985) to diffusion models. In spite of their great success in editing, their diffusion models learn the distribution of the learned embeddings in VAE or autoencoder, not the images. Kim & Ye (2021) proposes another strategy: fine-tuning a whole diffusion model for image editing. It shows valid performance but it requires each fine-tuned model corresponding each attribute.

In comparison, Asyrp enables outstanding manipulation without high computation, specifically designed architectures, or fine-tuning whole models.

Meanwhile, generative adversarial network Goodfellow et al. (2020) address their latent space for image editing (Ling et al. (2021), Härkönen et al. (2020), Chefer et al. (2021), Shen et al. (2020),

Yüksel et al. (2021), Patashnik et al. (2021), Gal et al. (2021), Dai et al. (2019), Xu et al. (2022)). However they have to conduct 'inversion' to their latent space for real image editing and 'GAN inversion' is often challenging and produces unexpected appearance changes.

On the contrary, Asyrp enables to use latent space of *real images* by nearly perfect easy inversion of DDIM.

B More discussion

In this section, we discuss the pros and cons of diffusion-model-based and GAN-based methods. And we provide guidelines for further improvements.

GAN-based latent manipulation methods Patashnik et al. (2021); Gal et al. (2021)require careful inversion from real images to latent codes for real image editing. On the contrary, our proposed method based on diffusion models has a powerful advantage; the sophisticated inversion method is not necessary. This means that we can obtain the latent code of an arbitrary real image even if the image is not in the trained domain. On the other hand, several inversion methods have been proposed for GANs to obtain the latent of the real image, and the corresponding latent manipulation method should be considered for each inversion method. For example, it is difficult to apply the method of editing in w space to the method of inversion using w^+ space.

However, GANs have the advantage of fast sampling. In addition, diffusion models have a relatively slow sampling time. Additionally, we have to be aware of the time steps of diffusion models, which is still less well known.

The advantage of being free from Inversion provides the following milestones. The manipulation in the latent of the diffusion models is the same as the editing in real images. It can be expanded to segmentation, clustering, classification, etc. in *h-space* for real-world images.

It would be an interesting research direction to employ previous techniques. Our method can be used in conjunction with gradient guidance methods. Although we do not focus on random sampling, ours works effectively for sampling with stochastic. (See § M.) It may bring more diverse methods to steer diffusion models.

h-space in the latent diffusion models such as stable diffusion, is another interesting research direction. The main contribution of our paper is only modifying $\mathbf{P}_t$ while preserving $\mathbf{D}_t$, and can be adapted with latent diffusion models. However, since the latent meaning may be different due to structural differences, research on this is needed.

Furthermore, all of the properties of *h-space* according to the time step has not been fully discussed so far. Research on them can be expected to expand further.

Limitations. Editing with Asyrp seldom yields changes in overall style or peripheral objects but edits attributes of the main object. Style transfer using frozen diffusion models is our future work.

Societal impact. Techniques for high-quality image manipulation such as Asyrp should be accompanied by social and/or technical solutions to prevent abuse.

C Proof of Theorem 1

Proof of **Theorem 1**. Let $\boldsymbol{\epsilon}_t^\theta$ be a predicted noise during the original reverse process at t and $\tilde{\boldsymbol{\epsilon}}_t^\theta$ be its shifted counterpart. Then, $\Delta \boldsymbol{x}_t = \tilde{\boldsymbol{x}}_{t-1} - \boldsymbol{x}_{t-1}$ is negligible where $\tilde{\boldsymbol{x}}_{t-1} = \sqrt{\alpha_{t-1}}\,\mathbf{P}_t(\tilde{\boldsymbol{\epsilon}}_t^\theta(\boldsymbol{x}_t)) + \mathbf{D}_t(\tilde{\boldsymbol{\epsilon}}_t^\theta(\boldsymbol{x}_t))$.

Define $\tilde{\boldsymbol{\epsilon}}_t^\theta(\boldsymbol{x}_t) = \boldsymbol{\epsilon}_t^\theta(\boldsymbol{x}_t) + \Delta\boldsymbol{\epsilon}_t$,$\{\beta_t\}_{t=1}^T = \{\beta_1 = \beta_{\text{min}}, ..., \beta_T = \beta_{\text{max}}\}$, and $\alpha_t = \prod_{s=1}^t (1 - \beta_s)$. Note that β_{max} is defined as a small value (e.g., $\beta_{\text{max}} = 0.001$) and $\{\beta_t\}_{t=1}^T$ are defined by a decreasing schedule from $\beta_T = \beta_{\text{max}}$ to $\beta_1 = \beta_{\text{min}} \approx 0$ (e.g., $\beta_{\text{min}} = 0.00001$). Then,

$$\tilde{\boldsymbol{x}}_{t-1} = \sqrt{\alpha_{t-1}}\,\mathbf{P}_t(\tilde{\boldsymbol{\epsilon}}_t^\theta(\boldsymbol{x}_t)) + \mathbf{D}_t(\tilde{\boldsymbol{\epsilon}}_t^\theta(\boldsymbol{x}_t)) \tag{10}$$

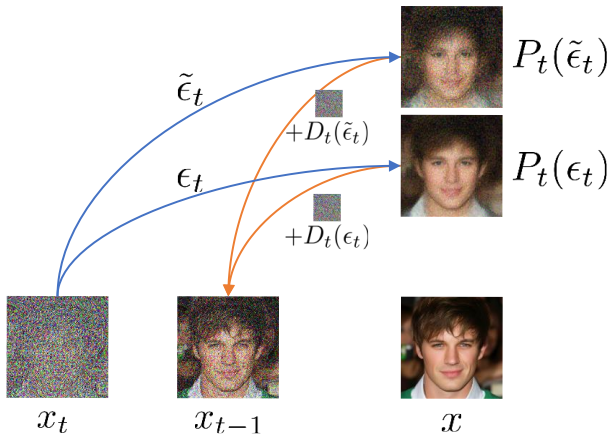

Figure 12: **Illustration of Theorem 1.** Upper blue line describes applying noise $\tilde{\boldsymbol{\epsilon}}_t = \boldsymbol{\epsilon}_t + \Delta\boldsymbol{\epsilon}_t$ to produce $\mathbf{P}_t(\tilde{\epsilon}_t) =$ the shifted predicted $\boldsymbol{x}_0$. However, the shift due to $\Delta\boldsymbol{\epsilon}_t$ is canceled out by the shift in $\mathbf{D}_t(\tilde{\boldsymbol{\epsilon}}_t)$ due to $\Delta\epsilon_t$. As a results, applying $\Delta\epsilon_t$ both on $\mathbf{P}_t$ and $\mathbf{D}_t$ brings identical outputs to the original.

$$= \sqrt{\alpha_{t-1}}\left(\frac{\boldsymbol{x}_t - \sqrt{1-\alpha_t}\left(\boldsymbol{\epsilon}_t^\theta(\boldsymbol{x}_t) + \Delta\boldsymbol{\epsilon}_t\right)}{\sqrt{\alpha_t}}\right) + \sqrt{1-\alpha_{t-1}} \cdot \left(\epsilon_t^{(\theta)}(\boldsymbol{x}_t) + \Delta\boldsymbol{\epsilon}_t\right) \tag{11}$$

$$= \sqrt{\alpha_{t-1}}\,\mathbf{P}_t(\boldsymbol{\epsilon}_t^\theta(\boldsymbol{x}_t)) + \mathbf{D}_t(\boldsymbol{\epsilon}_t^\theta(\boldsymbol{x}_t)) - \frac{\sqrt{\alpha_{t-1}}\sqrt{1-\alpha_t}}{\sqrt{\alpha_t}} \cdot \Delta\boldsymbol{\epsilon}_t + \sqrt{1-\alpha_{t-1}} \cdot \Delta\boldsymbol{\epsilon}_t \tag{12}$$

$$= \boldsymbol{x}_{t-1} + \left(-\frac{\sqrt{1-\alpha_t}}{\sqrt{1-\beta_t}} + \sqrt{1-\alpha_{t-1}}\right) \cdot \Delta\boldsymbol{\epsilon}_t \tag{13}$$

$$= \boldsymbol{x}_{t-1} + \left(-\frac{\sqrt{1-\alpha_t}}{\sqrt{1-\beta_t}} + \frac{\sqrt{1-\prod_{s=1}^{t-1}(1-\beta_s)}\sqrt{1-\beta_t}}{\sqrt{1-\beta_t}}\right) \cdot \Delta\boldsymbol{\epsilon}_t \tag{14}$$

$$= \boldsymbol{x}_{t-1} + \left(\frac{\sqrt{1-\alpha_t-\beta_t} - \sqrt{1-\alpha_t}}{\sqrt{1-\beta_t}}\right) \cdot \Delta\boldsymbol{\epsilon}_t \quad \because \alpha_t = \prod_{s=1}^{t}(1-\beta_s) \tag{15}$$

$$\therefore \Delta\boldsymbol{x}_t = \tilde{\boldsymbol{x}}_{t-1} - \boldsymbol{x}_{t-1} = \left(\frac{\sqrt{1-\alpha_t-\beta_t} - \sqrt{1-\alpha_t}}{\sqrt{1-\beta_t}}\right) \cdot \Delta\boldsymbol{\epsilon}_t \text{ is negligible} \quad \because \beta_t < \beta_{max} \tag{16}$$

□

D ADDITIONAL SUPPORTS FOR *h-space* WITH ASYRP

D.1 RANDOM PERTURBATION ON ϵ-*space* WITHOUT ASYRP

In § 3.1, we argue that if both $\mathbf{P}_t$ and $\mathbf{D}_t$ are shifted, we can not manipulate $\boldsymbol{x}_0$. In Figure 13, we do not observe the noticeable difference between (a) and (b) which are the result of the original reverse process of DDIM and the one with shifting both terms, respectively.

D.2 ROBUSTNESS AND SEMANTICS IN *h-space* AND ϵ-*space* WITH ASYRP

In § 3.2, we also argue that *h-space* is more robust than ϵ-space with Asyrp. In Figure 13, we observe that small random noise $z \sim \mathcal{N}(0, \mathbf{I})$ in ϵ-space degrades the resulting image without semantic changes (c) and much larger random noise in *h-space* yields random semantic changes without severe artifacts (d).

Note that diffusion models are designed as latent variable models with learned Gaussian transitions and the reverse process should also be close to Gaussian. Based on the assumption, we manage ϵ_t^θ to follow the original Gaussian distribution as follows. Adding $z \sim \mathcal{N}(0, \sigma\mathbf{I})$ to ϵ_t^θ expands the distribution of the predicted noise and may produce distorted images. To preserve the distribution, we scale $\tilde{\epsilon}_t^\theta = (\epsilon_t^\theta + z)/\sqrt{1^2 + \sigma^2}$. Still, the resulting images are almost identical compared to the original images where $\tilde{\epsilon}_t^\theta = \epsilon_t^\theta + z$ as shown in Figure 13. It is no wonder that the scaling does not improve the distorted results since the additive random noise disturbs the denoising operation of the predicted random noise.

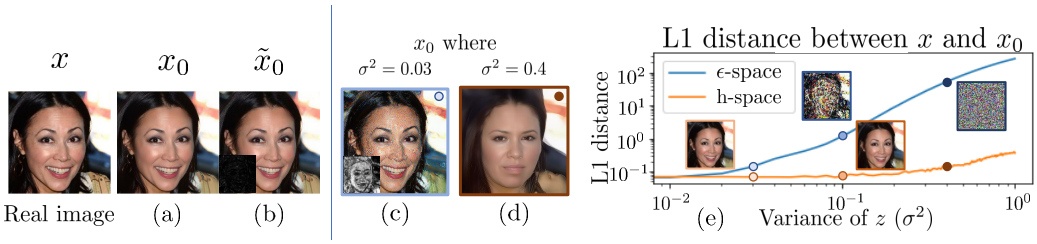

Figure 13: (a) The reconstructed image by the original DDIM inversion process which is almost indistinguishable to the real image. (b) The result from adding random noise z both on $\mathbf{P}_t$ and $\mathbf{D}_t$. (a) looks identical to (b). The insets of (b, c) depict the full SSIM image from (a). It shows that simply shifting ϵ_t^θ without Asyrp does not affect the result. (c) Adding $z \sim \mathcal{N}$ to ϵ-space with Asyrp easily degrades image with little semantic change. (d) Adding $z \sim \mathcal{N}$ to h-space with Asyrp yields random semantic change without image degradation. (e) Correlation between image degradation and noise strength in the two spaces.

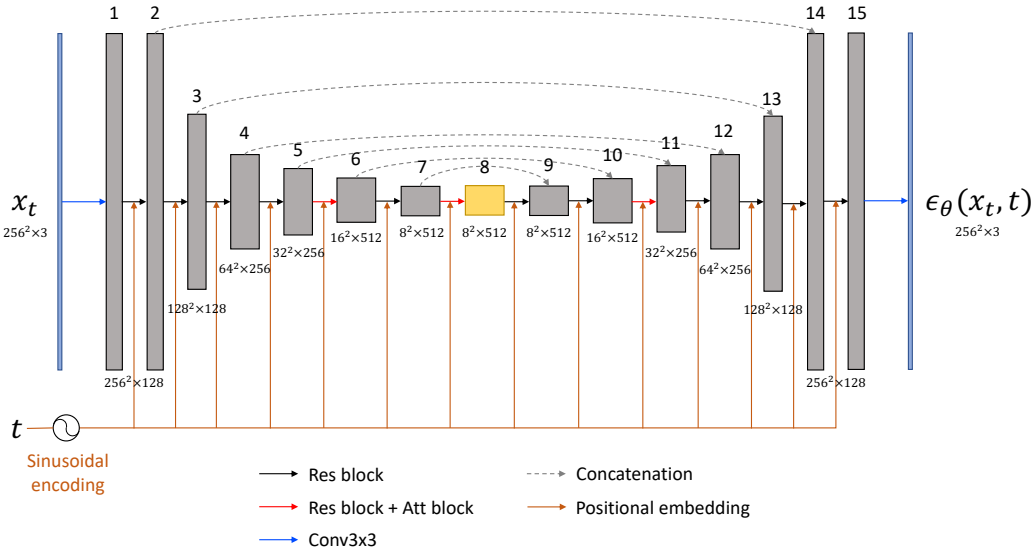

Figure 14: **Location of *h-space*.** The U-Net architecture of diffusion models outputs 256×256 images. Each layer is indexed with a number along the operating sequence of the model. The 8th layer is our *h-space* which is not directly influenced by a skip connection.

D.3 CHOICE OF *h-space* IN U-NET

As shown in Figure 14, there are many other candidates for *h-space* in the architecture. Among the layers, we choose the 8th layer, the bridge of the U-Net based architecture. The layer is not influenced by any skip connection, has the smallest spatial dimension with compressed information, and is located just before the upsampling blocks. Thus, we assume that it could possibly be considered as the most suitable latent embedding. To confirm the assumption, we train $\boldsymbol{f}_t$ on the other layers. The results are shown in Figure 15. We carefully tuned the training hyperparameters (λ_{CLIP} and λ_{recon}) for fair comparison. The 1st to the 6th layers hardly bring visible changes. The 7th and 9th layers bring not only the desired changes but also difficulty in finding optimal hyperparameters. After the 9th layer, the results bear severe artifacts.

E IMPLICIT NEURAL DIRECTIONS

Figure 16 illustrates the neural implicit function $\boldsymbol{f}_t$. It has only two 1x1 convolution layers with 512 channels.

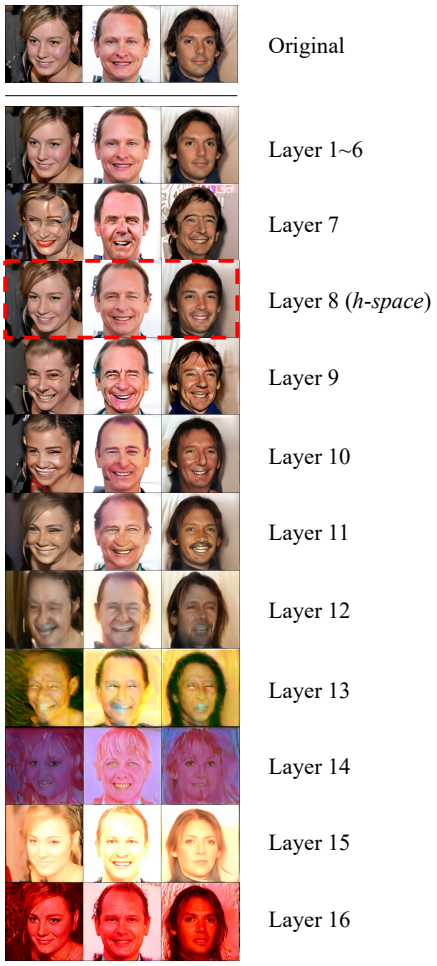

Figure 15: **Exhaustive enumeration over the choices for semantic latent space.** We show the result of the training data. We observe that the eighth layer (*h-space*) of the U-net suits the best for the semantic latent space.

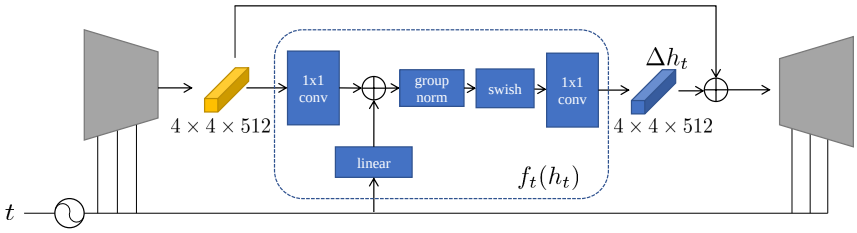

Figure 16: **Illustration of f_t.** We use group norm and swish following DDPM.

F Quality improvements by non-accelerated sampling with scaled Δh_t

Figure 17 shows the quality improvements by non-accelerated sampling with scaled $\Delta \boldsymbol{h}_t$ described in § 3.4. Even with different number of inference steps, we observe similar changes of an attribute if we preserve the sum of $\Delta \boldsymbol{h}_t$. This scaling technique allows non-accelerated sampling with 1000 steps for the models trained by accelerated training with 40 steps. Using non-accelerated sampling

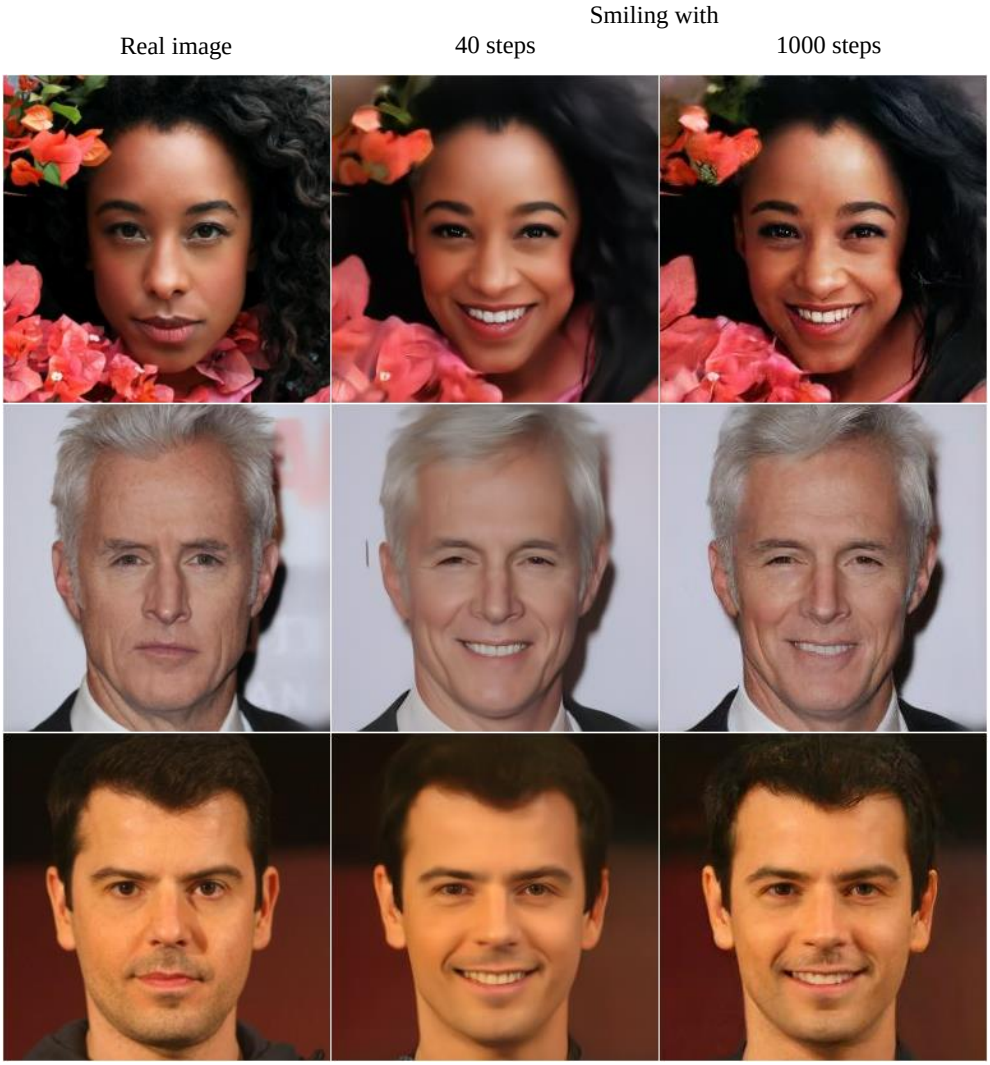

Figure 17: **Quality improvements by non-accelerated sampling with scaled $\Delta \boldsymbol{h}_t$.** We observe quality improvements by non-accelerated (1000-step) sampling with scaled $\Delta \boldsymbol{h}_t$ from accelerated (40-step) training described in § 3.4. Please zoom in for detailed comparison.

with scaled $\Delta \boldsymbol{h}_t$ leads to the same magnitude of manipulation and higher-quality images. In our experiments, it takes about 1.5 seconds to sample for 40 steps and 40 seconds for 1000 steps.

G EDITING STRENGTH AND EDITING FLEXIBILITY

G.1 EDITING STRENGTH AND t_{edit}

Figure 18 shows the results according to t_{edit}. If t_{edit} is too high, the length of the editing process becomes too short resulting in insufficient changes. On the contrary, too low t_{edit} causes excessively unnecessary manipulation from the long editing process.

We observe that t_{edit} is one of the important hyperparameters. We argue that the formula for choosing t_{edit} using editing strength is reasonable because it applies to all five different datasets despite its sensitivity, even though the choice of $\text{LPIPS} = 0.33$ is empirical. We provide ablation of thresholds in Figure 22.

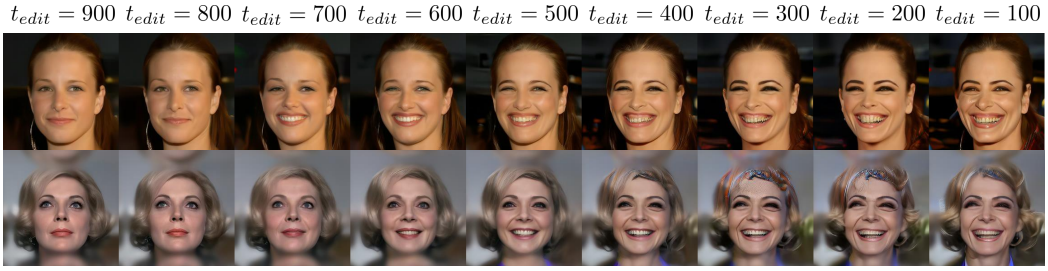

Figure 18: **Importance of choosing proper t_{edit}.** We explore various t_{edit} with `smiling`. Too short editing interval struggles to manipulate attributes. Excessive editing strength results in degraded images.

Additionally, these results imply why we need to use sufficiently low t_{edit} in the unseen domains. Editing interval with insufficient editing strength struggles to escape from the training domain.

Dataset	src_txt	trg_txt	CLIP similarity	t_{edit}	t_{boost}
CelebA-HQ	Person	Young person	0.905	515	167
	Face	Smiling face	0.899	513	167
	Face	Sad face	0.894	513	167
	Face	Angry face	0.892	512	167
	Face	Tanned face	0.886	512	167
	Face	Disgusted face	0.880	511	167
	Person	Person with makeup	0.875	509	167
	Human	Zombie	0.868	506	167
	Person	Person with bald head	0.861	505	167
	Person	Person with curly hair	0.835	499	167
	Human	Neanderthal	0.802	490	167
	Person	Mark Zuckerberg	0.797	489	167
	Person	Nicolas Cage	0.710	461	167
	Human	Painting in the style of Pixar	0.667	446	167
	Photo	Painting in Modigliani style	0.565	403	167
	Photo	Self-portrait by Frida Kahlo	0.443	321	167
LSUN-church	Church	Gothic Church	0.912	371	293
	Church	Temple	0.898	367	293
	Church	Department store	0.841	349	293
	Church	Wooden House	0.793	333	293
	Church	Ancient traditional Asian tower	0.784	330	293
	Church	Red brick wall Church	0.774	326	293
	Church	Factory	0.702	301	293
LSUN-bedroom	Bedroom	Princess Bedroom	0.912	370	221
	Bedroom	Hotel Bedroom	0.917	371	221
AFHQ	Dog	Happy Dog	0.883	430	167
	Dog	Sleepy Dog	0.866	422	167
	Dog	Angry Dog	0.860	419	167
	Dog	Wolf	0.850	412	167
	Dog	Yorkshire Terrier	0.690	302	167
METFACES	Painting of a person	Painting of a Sad person	0.921	330	180
	Painting of a person	Painting of a Smiling person	0.908	320	180
	Painting of a person	Painting of a Disgusted person	0.879	291	180

Table 2: Prompts, CLIP similarity, t_{edit}, and t_{boost} for all attributes in the experiments.

G.2 EDITING FLEXIBILITY AND t_{boost}

Table 2 shows the prompts, t_{edit}, and t_{boost}. Intuitively, the attributes with larger visual changes have smaller cosine similarity and require longer editing interval. Figure 19 shows the average $\text{LPIPS}(\boldsymbol{x}, \mathbf{P}_t)$ and $\text{LPIPS}(\boldsymbol{x}, \boldsymbol{x}_t)$ of 100 samples on all datasets. Note that t_{edit} and t_{boost} differ across datasets and attributes, and they are chosen by the formulas in § 4. We provide ablation of t_{boost} in Figure 23.

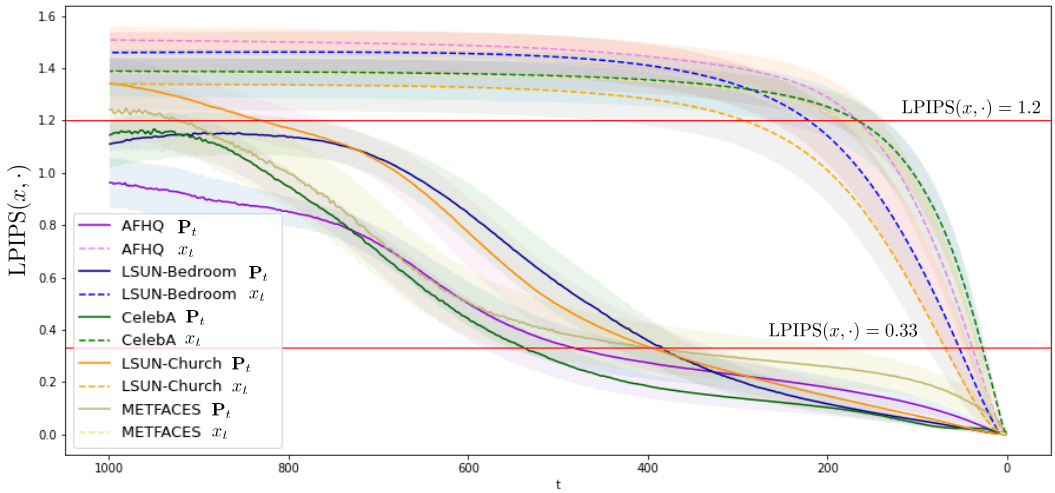

Figure 19: **Average** $\mathrm{LPIPS}(\boldsymbol{x}, \mathbf{P}_t)$ **and** $\mathrm{LPIPS}(\boldsymbol{x}, \boldsymbol{x}_t)$ **of 100 samples on all datasets.**

H QUALITY BOOSTING

We validate the effectiveness of our quality boosting (§ 4.2) in the original DDIM process and in Asyrp.

Figure 20 shows the effect of quality boosting with the original DDIM reverse process. Although the reverse process of DDIM has a nearly-perfect inversion property, we observe some noise by zooming in. Our quality boosting improves the quality of a sample and concurrently keeps nearly perfect inversion property. We observe that t_{boost} is not sensitive, but the larger interval brings the less preservation.

Figure 21 shows quality improvements by our quality boosting in Asyrp.

I ALGORITHM

Figure 24 illustrates generative process. Algorithm 1 and 2 describe training algorithm and inference algorithm of Asyrp, respectively.

J TRAINING DETAILS

J.1 LOSS COEFFICIENTS

Table 3 reports loss coefficients for each attribute. λ_{CLIP}s near 0.8 are suitable for most in-domain attributes. For unseen domains, higher coefficient leads to more noticeable changes.

J.2 TRAINING WITH RANDOM SAMPLING INSTEAD OF THE TRAINING DATASETS

Apparently, for training, inverting real-images can be replaced by random sampling. It refers to using $\boldsymbol{x}_T \sim \mathcal{N}(0, \mathbf{I})$ instead of $\boldsymbol{x}_T = q(\boldsymbol{x}_0) \cdot \prod_{t=1}^{T} q\left(\boldsymbol{x}_t \mid \boldsymbol{x}_{t-1}\right)$ where $\boldsymbol{x}_0 \sim p_{data}(x)$. It allows us to train Asyrp only with the pretrained network and without extra dataset. Using random samples has tradeoff between preservation of contents and possible amount in editing. It take advantages when a target attribute requires large amount changes. We assume that the inversion of real-image is in the long tail of a Gaussian distribution because of realistic background or detailed clothes. On the other hand, random noise is considered to be closer to the mean of the normal, so it is easier to find directions. It can easily bring larger changes but also easily alter the contents. On the contrary, training with inversion shows the opposite property.

Real image | w/o Quality boosting | w/ Quality boosting

Figure 20: **Ablation study of quality boosting on the original DDIM process *without* Asyrp**. Our quality boosting enhances fine details and prevents images from being noisy in the original DDIM process. Please zoom in for detailed comparison.

Smiling

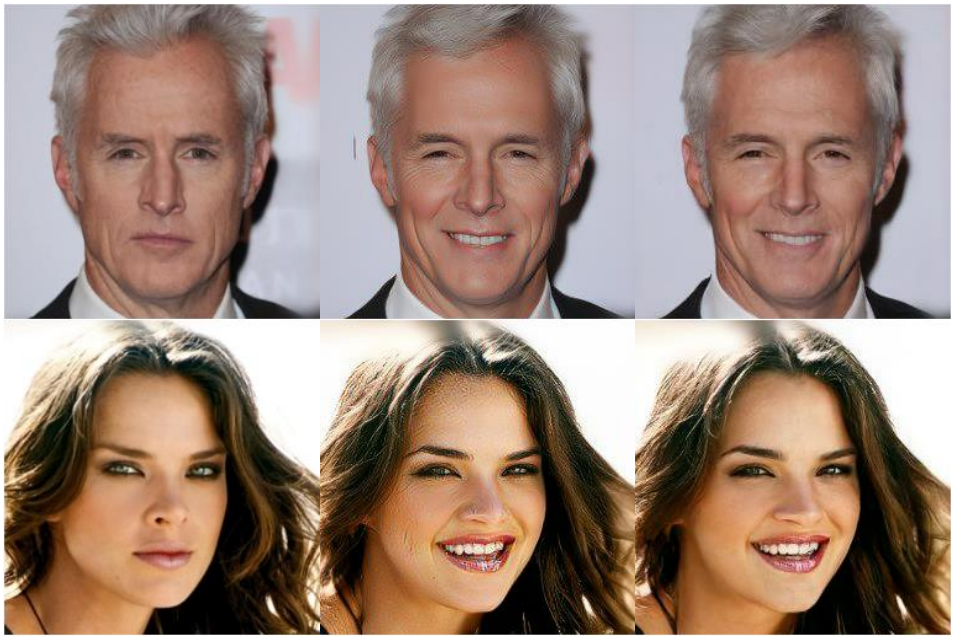

Real image | w/o Quality boosting | w/ Quality boosting

Figure 21: **Ablation study of quality boosting with Asyrp.** Our quality boosting enhances fine details and prevents images from being noisy. Note that the source of degradation is DDIM process, not Asyrp, confirmed in Figure 20. Please zoom in for detailed comparison.

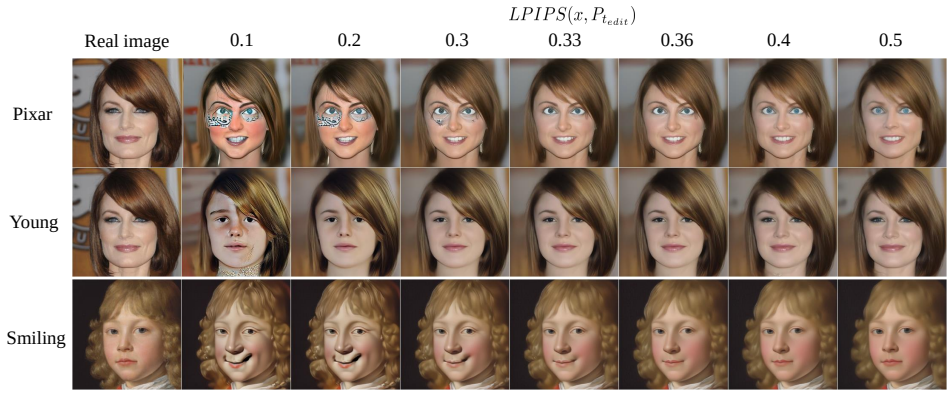

Figure 22: **Analyzing the effect of the hyperparameters** The figure shows that the calculated parameter works effectively as the maximum boundary of editing while maintaining the quality of the image.

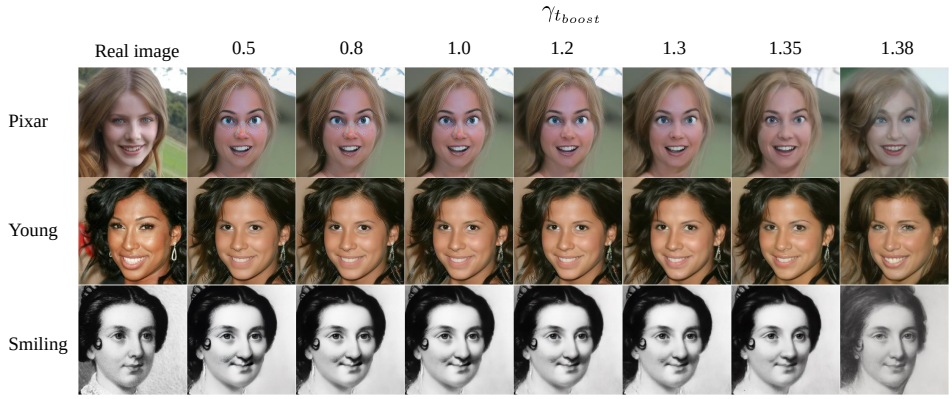

Figure 23: **Analyzing the effect of the hyperparameters** We observe that the quality of results has robustness to $\gamma_{t_{\text{boost}}}$, except for too large $\gamma_{t_{\text{boost}}}$.

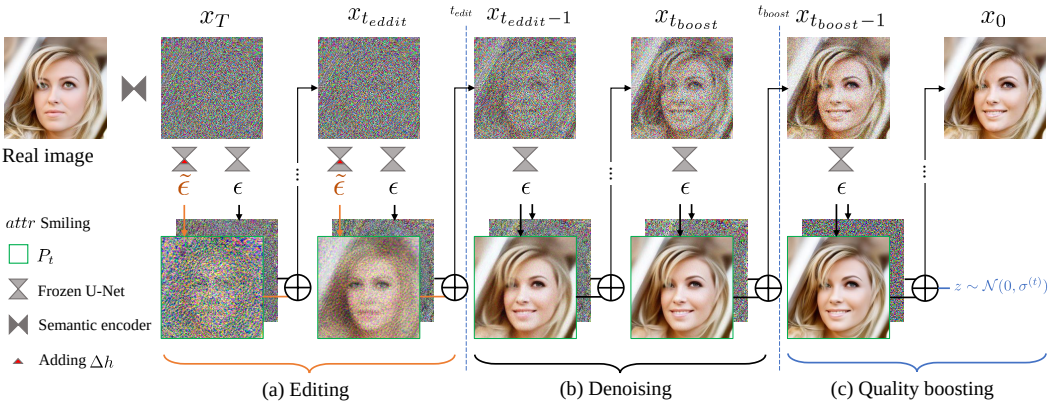

Figure 24: **Overview of our generative process.**

We train $\boldsymbol{f}_t$ with random sampling for attributes whose identity preservation is not important to take advantage of these properties. The rightmost column in Table 3 shows the choices.

Algorithm 1: Editing(Inference)

Input: x_0(Input image), $\{f_t^i\}_{i=1}^M$(M Neural implicit functions for M attributes), $\{c_i\}_{i=1}^M$(user defined M scaling coefficients for M attributes), ϵ_θ (frozen pretrained model), S_{for} (# of inversion steps), S_{gen}(# of inference steps), t_{edit} (computed from § 4.1), t_{boost} (computed from § 4.2)

Function `Editor` (x_0, ϵ_θ, $\{c_i\}_{i=1}^M$, S_{for}, S_{gen},$*$) **:**

`// step 1: Semantic encoding`

Define $\{\tau_s\}_{s=1}^{S_{for}}$ s.t $\tau_1 = 0$, $\tau_{S_{for}} = T$

for $s = 1, 2, ..., S_{for} - 1$ **do**

$\epsilon \leftarrow \epsilon_\theta(x_{\tau_s}, \tau_s)$

$x_{\tau_{s+1}} = \sqrt{\alpha_{\tau_s}} x_{\tau_s} + \sqrt{1 - \alpha_{\tau_s}} \epsilon$

`// step 2: Manipulation`

Define $\{\tilde{\tau}_s\}_{s=1}^{S_{gen}}$ s.t $\tilde{\tau}_1 = 0$, $\tilde{\tau}_{S_{edit}} = t_{edit}$, $\tilde{\tau}_{S_{noise}} = t_{\text{boost}}$ and $\tilde{\tau}_{S_{gen}} = T$

$\tilde{x}_{\tilde{\tau}_{S_{gen}}} = x_{\tilde{\tau}_{S_{for}}}$

for $s = S_{gen}, S_{gen} - 1, ..., 2$ **do**

`// phase 1: editing`

if $s \geq S_{edit}$ **then**

Extract feature map $h_{\tilde{\tau}_s}$ from $\epsilon_\theta(\tilde{x}_{\tilde{\tau}_s})$

$\Delta h_{\tilde{\tau}_s} = \frac{S_{for}}{S_{gen}} (\sum_{i=1}^M c_i f_{\tilde{\tau}_s}^i (h_{\tilde{\tau}_s}))$

$\tilde{\epsilon} = \epsilon_\theta(\tilde{x}_{\tilde{\tau}_s} | \Delta h_{\tilde{\tau}_s})$

$\epsilon = \epsilon_\theta(\tilde{x}_{\tilde{\tau}_s})$

$\sigma_{\tilde{\tau}_s} = 0$

`// phase 2: denoising`

else if $s \geq S_{noise}$ **then**

$\tilde{\epsilon} = \epsilon = \epsilon_\theta(\tilde{x}_{\tilde{\tau}_s})$

$\sigma_{\tilde{\tau}_s} = 0$

`// phase 3: quality boosting`

else

$\tilde{\epsilon} = \epsilon = \epsilon_\theta(\tilde{x}_{\tilde{\tau}_s})$

$\sigma_{\tilde{\tau}_s} = \sqrt{(1 - \alpha_{\tilde{\tau}_s - 1}) / (1 - \alpha_{\tilde{\tau}_s})} \sqrt{1 - \alpha_{\tilde{\tau}_s} / \alpha_{\tilde{\tau}_s - 1}}$

$z \sim N(0, 1)$

$\tilde{x}_{\tilde{\tau}_{s-1}} = \sqrt{\alpha_{\tilde{\tau}_{s-1}}} \left(\frac{\tilde{x}_{\tilde{\tau}_s} - \sqrt{1 - \alpha_{\tilde{\tau}_s}} \tilde{\epsilon}}{\sqrt{\alpha_{\tilde{\tau}_s}}} \right) + \sqrt{1 - \alpha_{\tilde{\tau}_{s-1}} - \sigma_{\tilde{\tau}_s}^2} \epsilon + \sigma_{\tilde{\tau}_s} z$

return $\tilde{x}_0$ (manipulated image)

K EVALUATION

K.1 USER STUDY

We conduct user study to compare the performance of Asyrp and DiffusionCLIP (Kim & Ye, 2021) on Celeba-HQ (Liu et al., 2015) and LSUN-church (Yu et al., 2015). We use official checkpoints provided by DiffusionCLIP except for some facial attributes whose checkpoint do not exist. We tried our best to tune their hyperparameters following the manual for fair comparison. Example images are shown in Figure 25-27.

We use `smiling` and `sad` for in-domain CelebA-HQ attributes, `Pixar` and `Neanderthal` for unseen-domain CelebA-HQ attributes, and `department store`, `ancient`, and `wooden` for LSUN-church.

In unseen domain and Lsun-church, we use official checkpoints provided by DiffusionCLIP. We also randomly select 8 images for each CelebA-HQ attribute and 12 images for each LSUN-church attribute.

Algorithm 2: Training Neural implicit function f_t

Input: ϵ_θ(pretrained model), $\{x_0^{(i)}\}_{i=1}^N$(images to precompute), f_t(Neural implicit function of an attribute), y_{src}(source text), y_{tar}(target text), S_{for}(# of inversion steps), K(# of training epochs), t_{edit} (computed from § 4.1), t_{boost} (computed from § 4.2)

`// step 1: Precompute latents`

Define $\{\tau_s\}_{s=1}^{S_{for}}$ s.t $\tau_1 = 0$,$\tau_{S_{for}} = T$
for $i = 1, 2, ..., N$ **do**
  for $s = 1, 2, ..., S_{for} - 1$ **do**
    $\epsilon \leftarrow \epsilon_\theta(x_{\tau_s}^{(i)}, \tau_s)$
    $x_{\tau_{s+1}}^{(i)} = \sqrt{\alpha_{\tau_s}} x_{\tau_s}^{(i)} + \sqrt{1 - \alpha_{\tau_s}}\epsilon$
  Save the latent $x_{\tau_{S_{for}}}^{(i)}$

$\tau_{S_{edit}} = t_{edit}$
`// step 2: Update` $\boldsymbol{f_t}$
for *epoch*$= 1, 2, ..., K$ **do**
  for $i = 1, 2, ..., N$ **do**
    Clone the latent $\tilde{x}_{\tau_{S_{for}}}^{(i)} = x_{\tau_{S_{for}}}^{(i)}$
    for $s = S_{for}, S_{for} - 1, ..., S_{edit}$ **do**
      Extract feature map h_{τ_s} from $\epsilon_\theta(\tilde{x}_{\tau_s}^{(i)})$
      $\Delta h_{\tau_s} = f_{\tau_s}(h_{\tau_s})$
      $P = \frac{\tilde{x}_{\tau_s}^{(i)} - \sqrt{1-\alpha_{\tau_s}}\epsilon_\theta(\tilde{x}_{\tau_s}^{(i)}|\Delta h_{\tau_s})}{\sqrt{\alpha_{\tau_s}}}$; $P_{src} = \frac{x_{\tau_s}^{(i)} - \sqrt{1-\alpha_{\tau_s}}\epsilon_\theta(x_{\tau_s}^{(i)})}{\sqrt{\alpha_{\tau_s}}}$
      $\tilde{x}_{\tau_{s-1}}^{(i)} = \sqrt{\alpha_{\tau_{s-1}}} P + \sqrt{1 - \alpha_{\tau_{s-1}}}\epsilon_\theta(\tilde{x}_{\tau_s}^{(i)})$
      $x_{\tau_{s-1}}^{(i)} = \sqrt{\alpha_{\tau_{s-1}}} P_{src} + \sqrt{1 - \alpha_{\tau_{s-1}}}\epsilon_\theta(x_{\tau_s}^{(i)})$
      $L_{total} \leftarrow \lambda_{CLIP} L_{direction}(P, y_{tar}, P_{src}, y_{src}) + \lambda_{recon}|\tilde{x}_{\tau_{s-1}}^{(i)} - x_{\tau_{s-1}}^{(i)}|$
      Take a gradient step on L_{total} and update f_t

We observe that DiffusionCLIP works better in changing the holistic style of images. At the same time, it is short of the ability to bring semantic changes and suffers noisy results and a lack of diversity. The problems would be caused by fine-tuning the whole diffusion model.

We use the following questions for the survey. 1) Quality: Which image quality do you think is better? (clear and less noisy) 2) Attribute: Which image do you think is "Attribute(e.g., Smiling) naturally"? 3) Overall: Which image do you think is better considering the above evaluation criteria?

As for LSUN-church, we provide a set of four images at once and add a question: 3) Diversity: Which group do you think has a more diverse style? 4) Overall: Which image do you think is better considering the above evaluation criteria?

K.2 Segmentation consistency and directional CLIP similarity

We compare Asyrp and DiffusionCLIP using directional CLIP similarity (S_{dir}) and segmentation-consistency (SC) following the protocols in DiffusionCLIP in Table 4 and Table 5. A pretrained CLIP (Radford et al., 2021) and segmentation models (Yu et al. (2018); Zhou et al. (2019; 2017); Lee et al. (2020)) are used to compute S_{dir} and SC, respectively. We choose three attributes (`smiling`, `sad`, `tanned`) for CelebA-HQ-in-domain, two attributes (`Pixar`,`Neaderthal`) for CelebA-HQ-unseen-domain and three attributes (`department store`, `ancient`, `red brick`) for LSUN-church.

For a fair comparison, we use official checkpoints of DiffusionCLIP and provide scores of the attributes (`tanned`, `red brick`) following Kim & Ye (2021). Regarding attributes without the official checkpoints (`smiling`,`sad`), we train DiffusionCLIP by ourselves with the official code.

Dataset	src_txt	trg_txt	λ_{CLIP}	λ_{recon}	from random noise
CelebA-HQ	Person	Young person	0.8	3	X
	Face	Smiling face	0.8	3	X
	Face	Sad face	0.8	3	X
	Face	Angry face	0.8	3	X
	Face	Tanned face	0.8	3	X
	Face	Disgusted face	0.8	3	X
	Person	Person with makeup	0.8	3	X
	Person	Person with curly hair	0.8	3	X
	Photo	Self-portrait by Frida Kahlo	0.5	3	O
	Human	Zombie	0.6	3	O
	Person	Nicolas Cage	0.8	3	O
	Human	Painting in the style of Pixar	0.8	3	O
	Photo	Painting in Modigliani style	0.8	3	O
	Human	Neanderthal	1.2	3	O
LSUN-church	Church	Gothic church	0.8	3	O
	Church	Temple	0.8	3	O
	Church	Department store	0.8	3	O
	Church	Wooden house	0.8	3	O
	Church	Ancient traditional Asian tower	0.8	3	O
	Church	Red brick wall Church	0.8	3	O
	Church	Factory	0.8	3	O
LSUN-bedroom	Bedroom	Princess bedroom	1.5	3	O
	Bedroom	Hotel bedroom	1.5	3	O
AFHQ-dog	Dog	Happy dog	1.5	3	O
	Dog	Sleepy dog	1.5	3	O
	Dog	Wolf	1.7	3	O
	Dog	Yorkshire terrier	2	3	O
METFACES	Painting of a person	Painting of a Sad person	1.5	3	X
	Painting of a person	Painting of a Smiling person	1.5	3	X
	Painting of a person	Painting of a Disgusted person	1.5	3	X

Table 3: The coefficients range from 0.5 to 0.8 for in-domain attributes. Unseen domains need slightly stronger λ_{CLIP}s. We also report which attributes we train with random noise sampling. The criterion is which attributes require relatively less maintenance of identity.

Figure 25: **Asyrp vs. DiffusionCLIP on CelebA-HQ in-domain attributes.** We observe that DiffusionCLIP struggles to change semantic facial attributes. Their official checkpoints do not exist and we ran careful hyperparameter tuning for training.

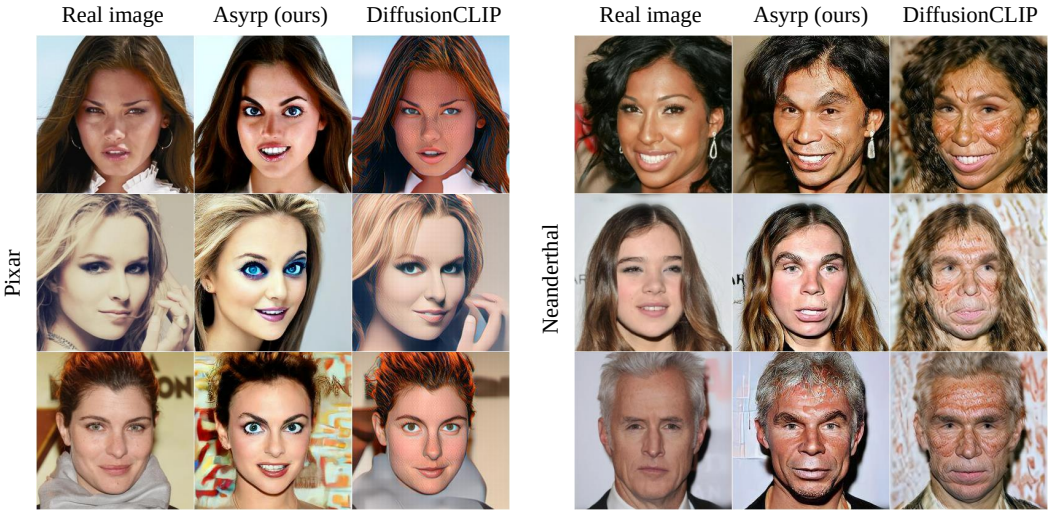

Figure 26: **Asyrp vs. DiffusionCLIP on CelebA-HQ unseen-domain attributes.** We use the official checkpoint provided by DiffusionCLIP. Asyrp works well even for the unseen-domains.

We use 100 samples per attribute. Asyrp outperforms DiffusionCLIP on S_{dir} for all attributes. On SC, DiffusionCLIP achieves better or competitive scores. Because DiffusionCLIP manipulates images mostly by focusing on texture or color while preserving structure and shape, it takes advantage of getting higher SC scores. However, in Figure 28, results of `smiling` show that it is not proper to edit attributes which require structural manipulation. Note that better SC scores do not guarantee better qualitative performance. Results of `Pixar` also show the similar tendency of each method. We allow more structural changes than DiffusionCLIP while editing. Lower SC of our method comes from *desirable* structural changes as shown in Figure 28.

$$\mathcal{S}_{\text{dir}}\left(\boldsymbol{x}_{\text{gen}}, y_{\text{tar}}; \boldsymbol{x}_{\text{ref}}, y_{\text{ref}}\right) := \frac{\langle \Delta I, \Delta T \rangle}{\|\Delta I\| \|\Delta T\|}, \tag{17}$$

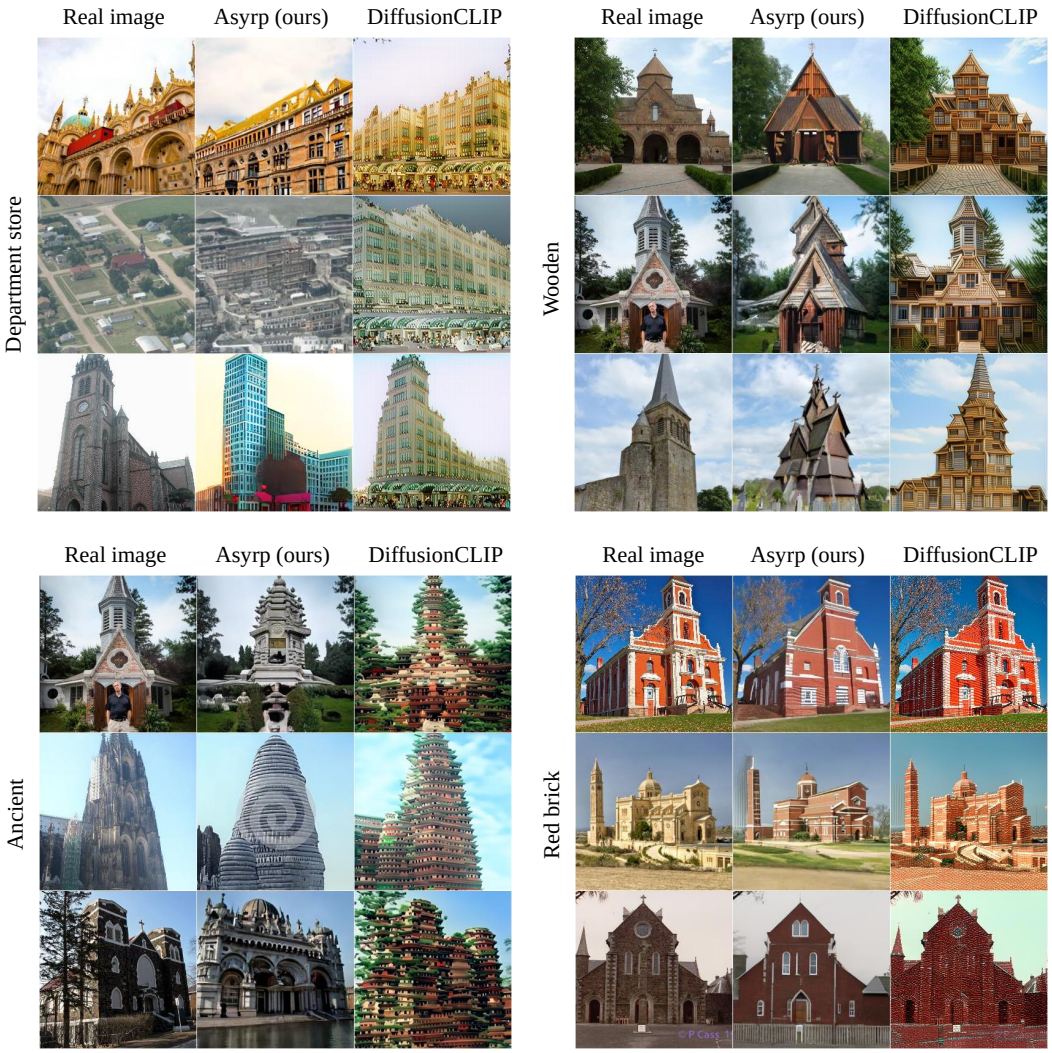

Figure 27: **Asyrp vs. DiffusionCLIP on LSUN-church.** Note that we use the official checkpoint provided by DiffusionCLIP. We observe DiffusionCLIP produces narrow range of styles while Asyrp produces diverse styles.

	CelebA-HQ-in-domain						CelebA-HQ-unseen-domain			
	Smiling		Sad		Tanned		Pixar		Neanderthal	
	S_{dir}	SC	S_{dir}	SC	S_{dir}	SC	S_{dir}	SC	S_{dir}	SC
Asyrp (ours)	**0.921**	89.02%	**0.964**	88.90%	**0.991**	85.71%	**0.956**	76.51%	**0.805**	79.03
DiffusionCLIP	0.813	**91.41%**	0.760	**89.93%**	0.888	**92.85%**	0.811	**89.91%**	0.661	**81.23%**

Table 4: **Quantitative evaluation on CelebA-HQ.**

L Directions

L.1 Global direction

Figure 29 and Figure 30 show that the effects of mean direction and global direction are quite similar with Δh_t by $\boldsymbol{f}_t$ in various attributes. We compute mean direction and global direction from 20 different images.

We argue that *h-space* is roughly homogeneous across samples and timesteps. However, we observe that *h-space* is not completely independent to the conditions especially on unseen-domain

	LSUN_church					
	Department store		ancient		red brick	
	S_{dir}	SC	S_{dir}	SC	S_{dir}	SC
Asyrp (ours)	**0.778**	**57.62%**	**0.943**	62.65%	**0.989**	**65.83%**
DIffusionCLIP	0.661	54.50%	0.907	**64.82%**	0.964	65.02%

Table 5: **Quantitative evaluation on LSUN-church.**

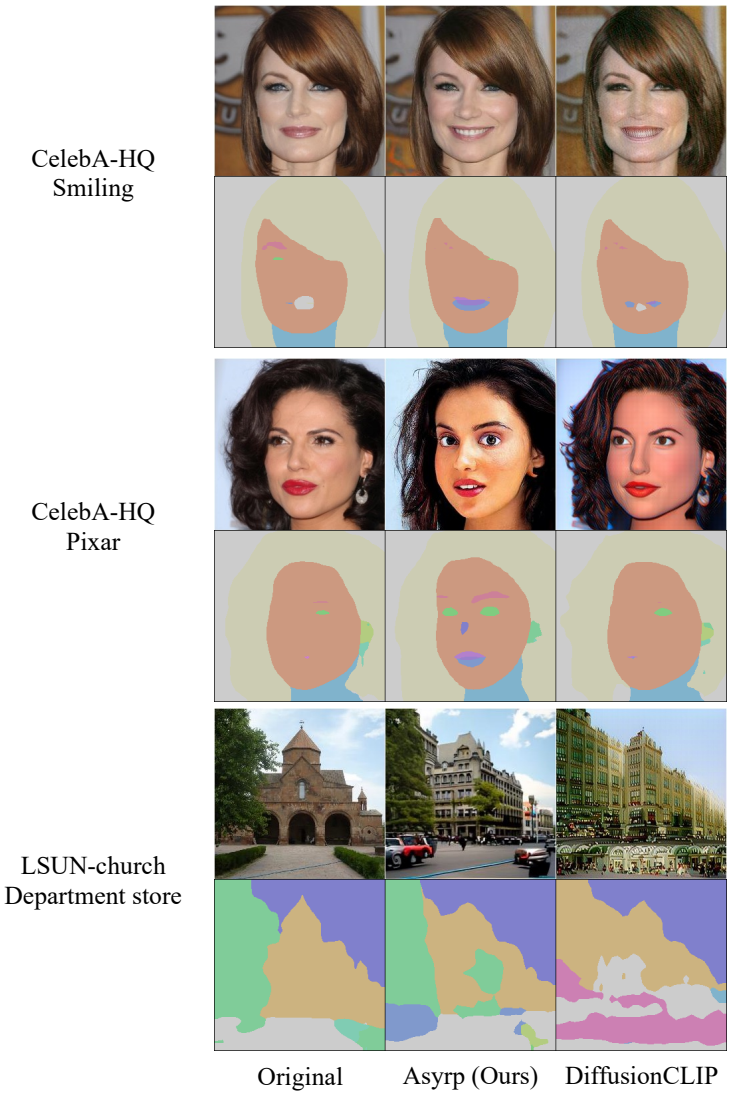

Figure 28: **Example segmentations for computing segmentation-consistency (SC).**

(See Figure 29). Note that unseen-domains require a longer editing interval with small t_{edit}. Therefore, we conjecture that the consistency of *h-space* decreases at the end of the generative process. It is supported by additional experiments that L2 distance between Δh_t and global direction gradually increases along with timesteps. We leave a more detailed analysis on *h-space* at different timesteps as a future work.

Figure 29: We compute mean direction and global direction from 20 other images on CelebA-HQ. The effect of mean direction and global direction are quite similar with Δh_t by f_t at diverse attributes.

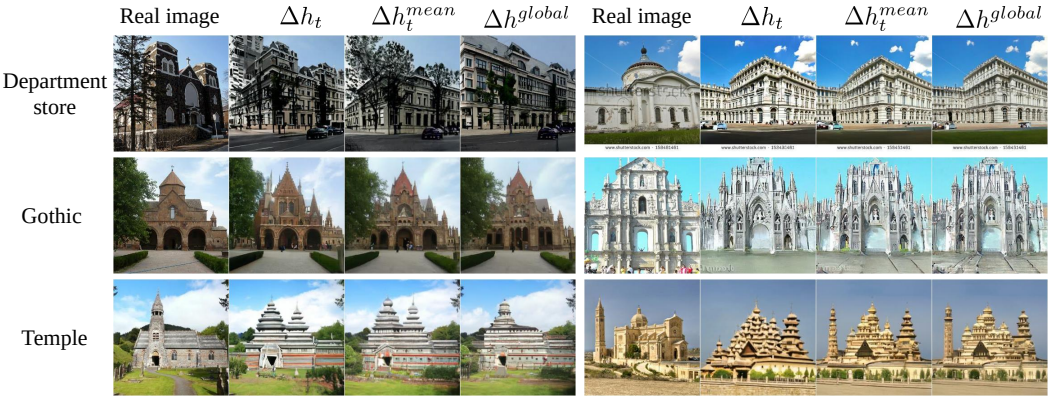

Figure 30: We obtain mean direction and global direction from 20 other images on LSUN-church. The effect of mean direction and global direction are quite similar with Δh_t by $\boldsymbol{f}_t$ at diverse attributes.

L.2 COMPARE THREE METHODS

In this section, we compare three methods: implicit neural direction f_t, optimized Δh_t, and optimized Δh^{global}.

Training time $f_t \approx \Delta h^{global} < \Delta h_t$

We have to optimize each Δh_t for each time step t. Additionally, it needs specific hyperparameters for each Δh_t, e.g., higher learning rates for larger t. On the contrary, time-consuming for f_t is similar to optimizing Δh^{global}.

Quality $f_t \approx \Delta h_t > \Delta h^{global}$

f_t and Δh_t, where directions can be obtained for each timestep, have the best quality. As can be shown in Figure 10, Δh^{global} is sometimes accompanied by slight differences in hair, etc.

Extensibility $f_t > \Delta h_t > \Delta h^{global}$

Δh_t can be obtained from f_t, and Δh^{global} can be obtained by aggregating Δh_t.

We opt to use f_t for above three advantages.

M RANDOM SAMPLING

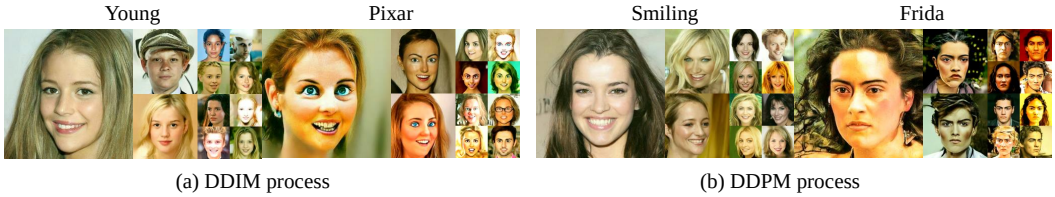

(a) DDIM process (b) DDPM process

Figure 31: **Uncurated random sampling.** We generate images from random noise with Asyrp. Although we do not focus on these results, Asyrp can be used for conditional sampling.

We conduct extra experiments: generating images with target attributes using Asyrp not from inversion but from random Gaussian noises. As a consequence, the generative process can be used for conditional random sampling. We provide the results in Figure 31. However, it is beyond the scope of this paper.

N MORE SAMPLES

N.1 MULTI-INTERPOLATION

Figure 32 provides mixed interpolation between multiple attributes. We observe that any interpolation with any attribute is possible.

N.2 MORE RESULTS ON ALL DATASETS

We provide more results on CelebA-HQ (Figure 33), LSUN-church (Figure 34), AFHQ, LSUN-bedroom, METFACES (Figure 35).

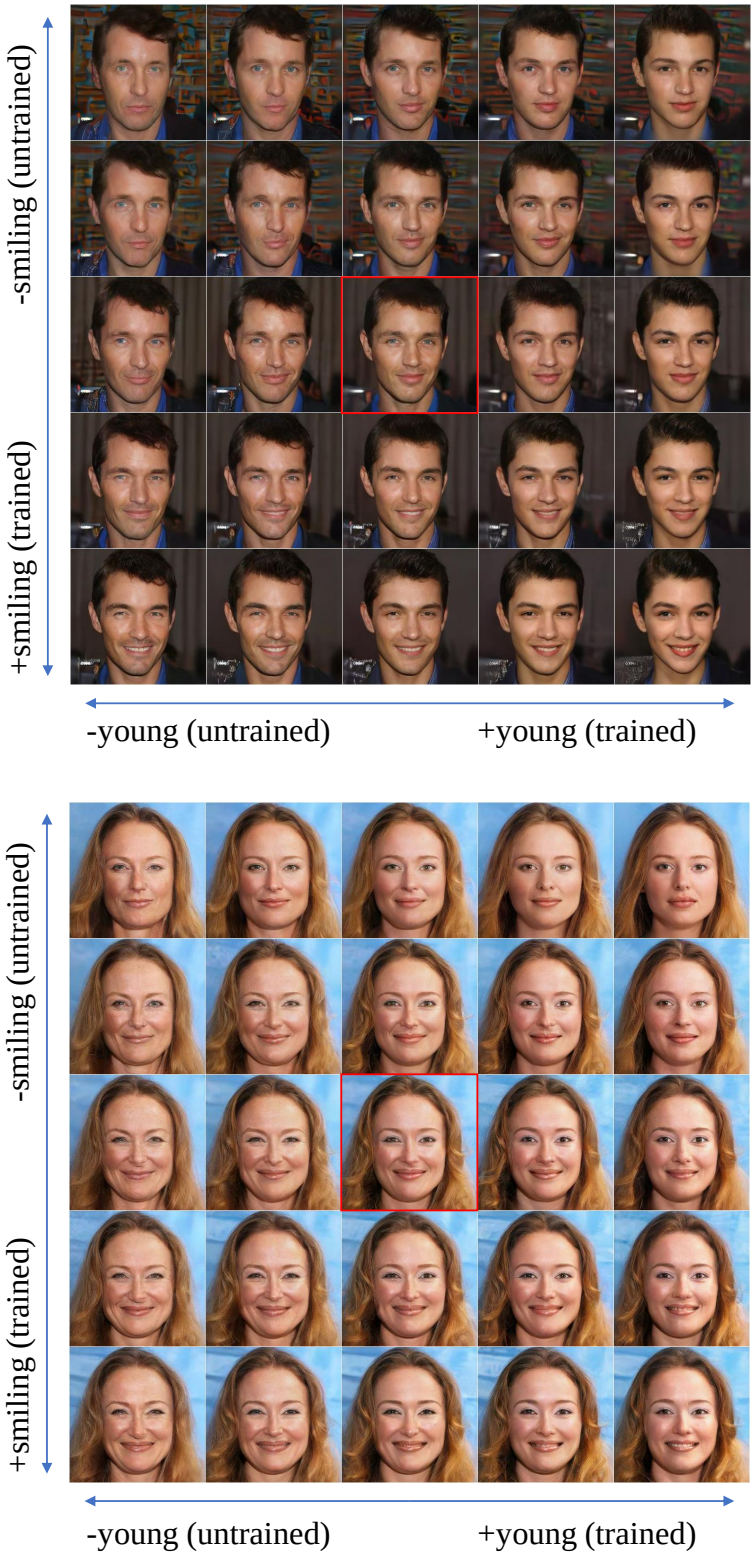

Figure 32: **Combination of multiple attributes.** The result shows that Asyrp works for combined Δh of `smiling` and `young`.

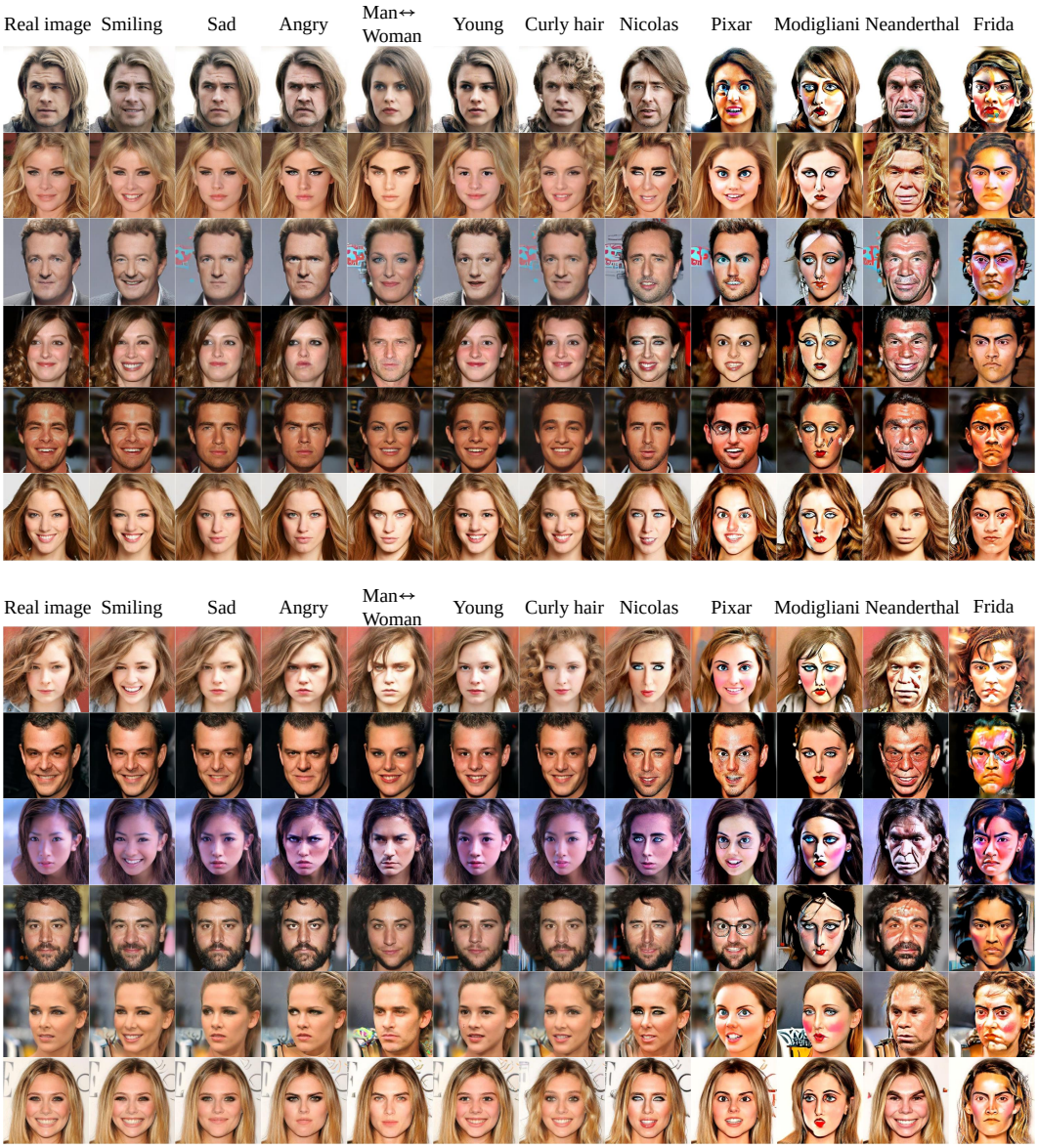

Figure 33: We provide more results on CelebA-HQ dataset.

Figure 34: We provide more results on LSUN-church dataset.

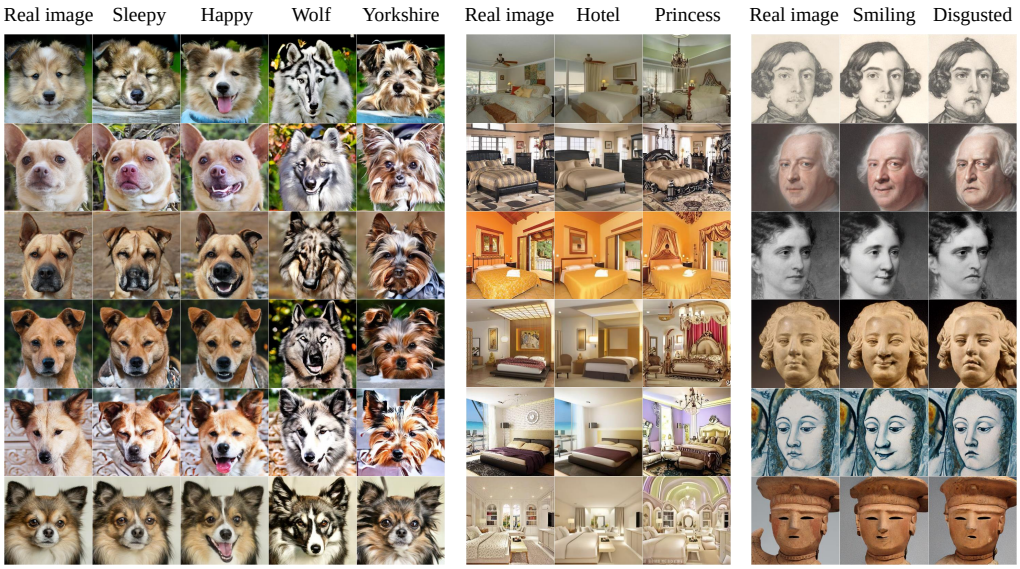

Figure 35: We provide more results on AFHQ, LSUN-bedroom and METFACES datasets respectively.